Antiviral Research 217 (2023) 105697

Contents lists available at ScienceDirect

Antiviral Research

journal homepage: www.elsevier.com/locate/antiviral

Diketo acid inhibitors of nsp13 of SARS-CoV-2 block viral replication

Angela Corona[a,1], Valentina Noemi Madia[b,1], Riccardo De Santis[c], Candida Manelfi[d], Roberta Emmolo[a], Davide Ialongo[b], Elisa Patacchini[b], Antonella Messore[b], Donatella Amatore[c], Giovanni Faggioni[c], Marco Artico[e], Daniela Iaconis[d], Carmine Talarico[d], Roberto Di Santo[b], Florigio Lista[c], Roberta Costi[b,**], Enzo Tramontano[a,*]

[a] *Dipartimento di Scienze della vita e dell'ambiente. Università degli Studi di Cagliari, Cittadella Universitaria di Monserrato, SS-554, Monserrato, Cagliari, Italy*
[b] *Dipartimento di Chimica e Tecnologie del Farmaco, Istituto Pasteur-Fondazione Cenci-Bolognetti, "Sapienza" Università di Roma, p.le Aldo Moro 5, I-00185, Rome, Italy*
[c] *Defense Institute for Biomedical Sciences, Via Santo Stefano Rotondo 4, 00184, Rome, Italy*
[d] *EXSCALATE - Dompé Farmaceutici SpA, via Tommaso De Amicis 95, 80131, Napoli, Italy*
[e] *Department of Sensory Organs, "Sapienza" Università di Roma, V.le Regina Elena 324, I-00161, Rome, Italy*

ARTICLE INFO

Keywords:
SARS-CoV-2 inhibition
nsp13
Helicase
Drug development
Unwinding inhibition

ABSTRACT

For RNA viruses, RNA helicases have long been recognized to play critical roles during virus replication cycles, facilitating proper folding and replication of viral RNAs, therefore representing an ideal target for drug discovery. SARS-CoV-2 helicase, the non-structural protein 13 (nsp13) is a highly conserved protein among all known coronaviruses, and, at the moment, is one of the most explored viral targets to identify new possible antiviral agents. In the present study, we present six diketo acids (DKAs) as nsp13 inhibitors able to block both SARS-CoV-2 nsp13 enzymatic functions. Among them four compounds were able to inhibit viral replication in the low micromolar range, being active also on other human coronaviruses such as HCoV229E and MERS CoV. The experimental investigation of the binding mode revealed ATP-non-competitive kinetics of inhibition, not affected by substrate-displacement effect, suggesting an allosteric binding mode that was further supported by molecular modelling calculations predicting the binding into an allosteric conserved site located in the RecA2 domain.

1. Introduction

The diffusion of the severe acute respiratory syndrome coronavirus 2 (SARS-CoV-2), first isolated in Wuhan in 2019, caused a pandemic with unprecedented socioeconomic impact (N. Chen et al., 2020; Wu et al., 2020), enlightening the need of new antiviral agents able to block viral replication. Most of the approved antiviral drugs target viral enzymes, most commonly proteases and polymerases, involved in key steps of the viral replication cycle.

Coronaviruses are (+)ssRNA viruses that possess a remarkably large RNA genome of around 30 kb (between 27.6 and 31 kb) (V'kovski et al., 2020) with two large open reading frames (ORF1a and ORF1b) in its 5′-region, encoding for 16 non-structural proteins (nsps) essential for viral replication.

The viral RNA-dependent RNA polymerase (RdRp, encoded by the non-structural protein 12 or nsp12) and the Mpro, encoded by nsp5, have been successfully targeted by approved inhibitors Remdesivir and Nirmaltrelvir, respectively (Gordon et al., 2020; Owen et al., 2021).

In particular, the large replication transcription complex of SARS-CoV-2 (RTC) comprises the RdRp assembled with two cofactor proteins, nsp7 and nsp8, and th and the viral helicasensp13, performing both unwinding and backtracking (J. Chen et al., 2020a; Gao et al., 2020; Malone et al., 2021). Other nsps are present such as the proofreading assembly module formed by nsp10/nsp14 nsp9, nsp10/14 and nsp16 shown to regulate the RNA 5′ cap synthesis and stabilize genomic RNAs (Minskaia et al., 2006). All are validated targets for antiviral discovery (Li et al., 2023).

The CoVs nsp13 is a multidomain enzyme of 601 amino acids that can unwind DNA or RNA in an NTP-dependent manner with a 5′-3′ polarity. It couples two C-terminal RecA ATPase domains, RecA1 (residues

---

* Corresponding author.
** Corresponding author.
E-mail addresses: roberta.costi@uniroma1.it (R. Costi), tramon@unica.it (E. Tramontano).
[1] These authors equally contributed to this work.

https://doi.org/10.1016/j.antiviral.2023.105697
Received 28 March 2023; Received in revised form 1 August 2023; Accepted 4 August 2023

260–442) and RecA2 (residues 443–596), characteristic of the 1B (SF1B) helicase superfamily (Saikrishnan et al., 2009; Singleton et al., 2007), with other three domains: the N-terminal zinc-binding domain (ZBD) (residues 1–100), essential for the helicase activity, a stalk domain (SD) (residues 101–150), and a 1B domain (residues 151–259) (J. Chen et al., 2020b; Hao et al., 2017; Jia et al., 2019; Lehmann et al., 2015).

Recently, the druggability and conservation of nsp13 binding pockets were analyzed by Gervasoni and colleagues (Gervasoni et al., 2020), and later Newman and co-workers (Newman et al., 2021) described two pockets of interest that are expected to be functionally relevant. These two pockets are: (i) the binding site occupied by AMP PNP, at the interface of domains 1A and 2A, and (ii) a pocket lined by domains 1A, 1B, and 2A which is occupied by the 5′-end of the RNA substrate in the SARS-CoV-2 transcription complex (Fig. 1). The analysis of conservation of these pockets among 27 sequences of nsp13 from α- and β-coronaviruses showed that 79% and 87% of residues lining the nucleotide and 5′-RNA sites, respectively, are conserved in all analyzed coronaviruses. On top of it, SARS-CoV-2 nsp13 shows a 99.8% of sequence identity with SARS-CoV-1, with only a single amino acid out 601 difference between nsp13s of SARS-CoV (I570) and SARS-CoV-2 (V570) (White et al., 2020; A.Wu et al., 2020). This could imply that small molecule inhibitors that bind to the pockets near conserved motifs may serve as broad-spectrum inhibitors and that previously found compounds targeting nsp13 in other CoVs species might be effective against SARS-CoV-2. Very recently, the structure of the nsp13-RTC complex has been solved by cryo-EM (Chen et al., 2022a; Yan et al., 2021), clarifying some dynamics of nsp13, and revealing a tight interplay between nsp13 and RdRp in the mechanism to switch between RNA synthesis or backtracking, thus opening new perspectives for antiviral targeting.

Several compounds have been reported to inhibit SARS-CoV-1 helicase activity (Keum and Jeong, 2012; Keum et al., 2013; Lee et al., 2009; Yu et al., 2012), and, very recently, also SARS-CoV-2 nsp13 has been actively explored as drug target, with several reports describing small molecules as inhibitors of SARS-CoV-2 helicase (Corona et al., 2022; Lu et al., 2022; Nizi et al., 2022; Zeng et al., 2021).

Diketo acid derivatives (DKAs) have been long studied as antiviral molecules active against several targets such influenza virus endonuclease (Tomassini et al., 1994), HIV-1 integrase (Wai et al., 2000), and HIV-1 RNase H (Sluis-Cremer et al., 2004; Tramontano et al., 2005; Costi et al., 2013b; Corona et al., 2014, 2016), able to block also viral replication. Following the first report on DKAs as micromolar inhibitors of the unwinding of SARS-CoV-1 nsp13 (Lee et al., 2009) and thanks to our longstanding expertise in the design and synthesis of DKA derivatives endowed with antiviral activity, we explored SARS-CoV-2 nsp13 as a target for our in-house library of DKAs, testing them on the recently established nsp13 enzymatic assay. Two indolyl DKA compounds, **1c** and **2c** (Costi et al., 2013a), emerged as promising hits, blocking both nsp13 catalytic activities in the low micromolar range. Therefore, we designed and synthesized a small set of structural analogues (Fig. 2, characterized by an indolyl core endowed with a diketohexenoic chain in 3-position, to further explore the SARS-CoV-2 nsp13 inhibition and the antiviral activities within this series of compounds.

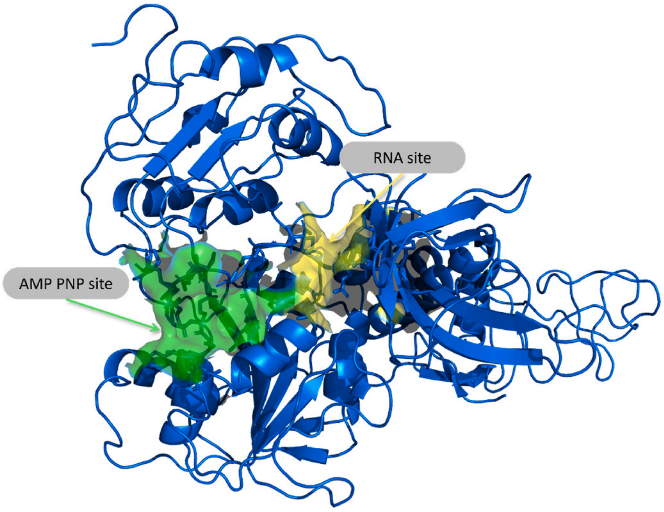

Fig. 1. Annotated binding sites occupied by AMP PNP, and by the 5′-end of the RNA substrate are reported in green and yellow surfaces respectively. Nsp13 structure is reported in blue cartoon.

2. Results

2.1. Chemistry

Compounds **1c** and **2c** were obtained as previously reported (Costi et al., 2013a). The synthesis of derivatives **1a,b** and **2a,b** is outlined in Scheme 1. Commercially available 1*H*-indole-3-carboxaldehyde was alkylated with 3,3-dimethylallyl bromide using NaH as a base to give the alkyl derivative **4a**, or arylated with 4-fluorophenylboronic acid following a microwave-assisted Chan-Lam cross-coupling procedure affording the *N*-aryl derivative **4b**. Condensation of **4a,b** with acetone in alkaline medium gave enones **3a,b** that underwent a Claisen-Schmidt condensation with diethyl oxalate using sodium ethoxide as a base, obtaining diketo esters **2a,b**. The subsequent base-catalyzed hydrolysis of ester derivatives **2a,b** afforded the corresponding diketo acids **1a,b**.

2.2. DKAs activity against SARS-CoV-2 nsp13 enzymatic functions

The indolyl DKA compounds, **1c** and **2c** (Costi et al., 2013a), and their structural analogues **1a,b** and **2a,b** (Fig. 2) were tested on both the SARS-CoV-2 nsp13 unwinding and ATPase associated activities (Table 1).

Compound SSYA10-001, that reported to inhibit SARS-CoV nsp13 (Adedeji et al., 2012), was used as a positive control, showing an IC_{50} value of 1.8 μM on SARS-CoV-2 nsp13 unwinding activity (Table 1). Compounds were also tested on the SARS-CoV-2 nsp13-associated ATPase activity using licoflavone C as a positive control (Table 1) (Corona et al., 2022). All assays were performed in the presence of 10 μg/ml of BSA and 180 μM TCEP in order to exclude the possibility of inhibition by non-specific aggregators. Results showed that the compounds were active against both enzymatic activities in the low micromolar range. Interestingly, about all compounds were active against unwinding in the same order of magnitude of SSYA10-001. Furthermore, all of them (except compound **1a**) proved to be more potent than licoflavone C (of ≈1.5–6 times). Among the tested compounds, derivatives **1b** and **2a** showed comparable inhibitory activities of the unwinding with that of SSYA10-001 (IC_{50} **1b** = 4.7 ± 1.1 μM; IC_{50} **2a** = 5.08 ± 0.01 μM) and very good potencies of inhibition against the nsp13-associated ATPase activity (IC_{50} **1b** = 8.2 ± 1.8 μM; IC_{50} **2a** = 3.88 ± 0.26 μM).

2.3. Antiviral activity

In the first set of experiments, was evaluated the effect of compounds on Vero cell viability. To this end, confluent monolayers of cells were treated with different concentrations (500–0.5 μg/mL) of indolyl DKA derivatives for 24, 48, and 72 h and then stained with trypan blue. Microscopic examination showed no significant mortality in cells treated with the compounds at a concentration of up to 264 μM. On the contrary, morphological alterations, loss of cell viability, and modification of the cell multiplication rate were observed at higher concentrations (data not shown). Based on results, the antiviral activity of DKAs against SARS-CoV-2 was tested through the plaque assay by using the compounds at concentrations ranging from 0.25 to 100 μM (Fig. 3A), using untreated-infected cells as a positive control of viral infection (10^3

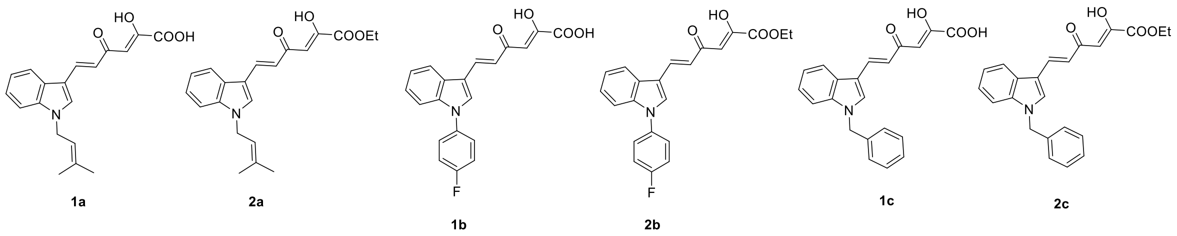

Fig. 2. Chemical structures of DKA derivatives 1a-c and 2a-c.

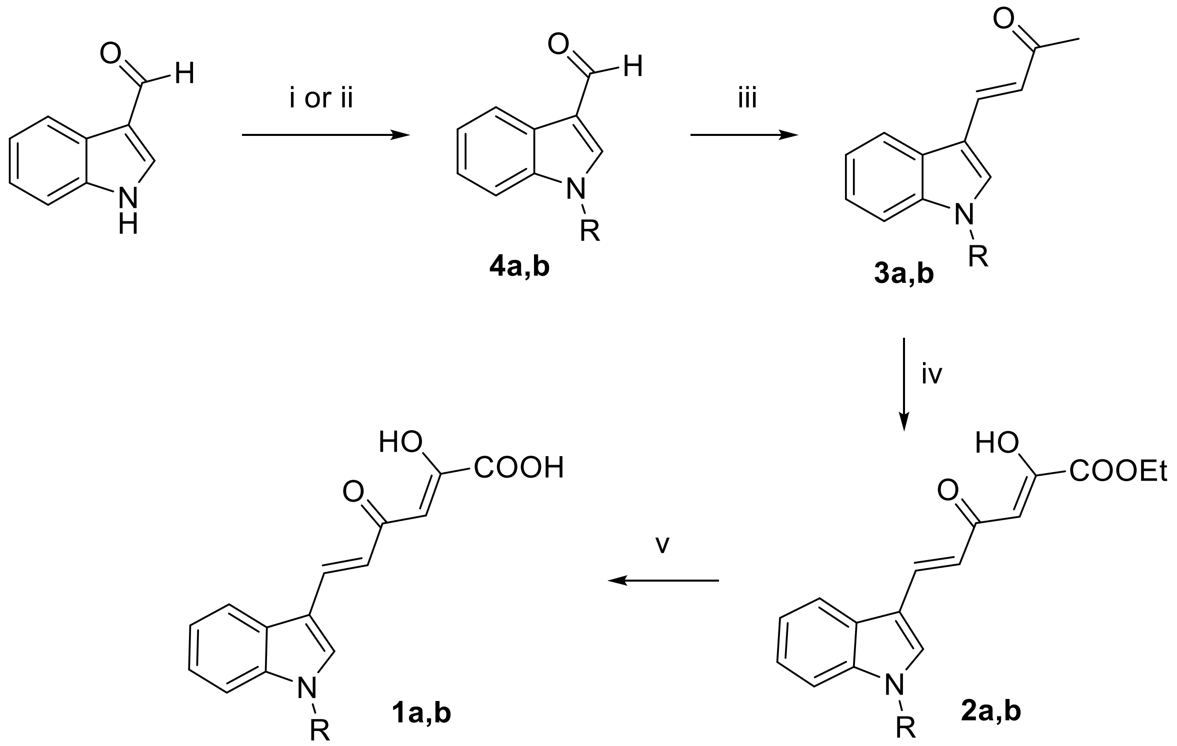

Scheme 1. Synthetic route to 1a,b and 2a,b derivatives. Reagents and conditions: (i) 3,3-dimethylallyl bromide, NaH, DMF dry, 1 h, 90 0 °C to rt, 89%; (ii) 4-fluorophenylboronic acid, cupric acetate, NMP/pyridine 1:1, microwave (60 W, 120 °C, 20 min), 48%; (iii) 5 N NaOH, acetone, 3–72 h, rt or 50 °C, 51–83%; (iv) diethyl oxalate, NaOEt, THF dry, 1.5 h, rt, 75–82%; (v) 1 N NaOH, THF/MeOH 1:1, 1.5 h, rt, 54–70%.

Table 1
Inhibition of SARS-CoV-2 nsp13 helicase-associated activities by DKAs.

Compound	Unwinding BSA-TCEP[a]IC$_{50}$ (μM)	ATPase BSA-TCEP-[b]IC$_{50}$ (μM)
1a	9.51 ± 2.5	26.8 ± 3.6
1b	4.7 ± 1.1	8.2 ± 1.8
1c	12.69 ± 4.9	12.8 ± 1.3
2a	5.08 ± 0.01	3.88 ± 0.26
2b	5.9 ± 0.3	13.6 ± 3.2
2c	5.49 ± 0.34	13.6 ± 2.5
SSYA10-001	1.8 ± 0.22	3.78 ± 1.5
Licoflavone C	7.8 ± 1.2	22.1 ± 1.4

Values are expressed as means ± the SD from at least two independent experiments, in triplicate.

[a] Compound concentration required to inhibit the SARS-CoV-2 nsp13-associated unwinding activity by 50%.

[b] Compound concentration required to inhibit the SARS-CoV-2 nsp13-associated ATPase activity by 50%.

pfu/mL), and the compound GC376, a known SARS-CoV-2 Mpro inhibitor as a positive control for viral replication inhibition (Ma et al., 2020). The data, reported in Table 2, indicate that all the compounds, except for **2a** and **2c**, were able to impair the infectivity of SARS-CoV-2, although with different efficiencies, causing a decrease of 2 logs on viral titer at the highest concentration tested.

To assess the *in vitro* inhibition potency of the selected compounds, the 50% effective concentration (EC$_{50}$) for each compound was estimated from the experimental curves. The values, reported in Fig. 3B, showed that compounds **1b** and **1c** (EC$_{50}$ values of 1.70 μM and 1.03 μM, respectively) inhibit more efficiently than **1a** and **2b** SARS-CoV-2 replication (EC$_{50}$ values of 4.54 μM and 16.07 μM respectively). In particular, the 95% confidence interval (CI) for each compound was: **1a**: 4.391–4.688; **1b**: 1.305–2.209; **1c**: 0.8116–1.291; **2b**: 12.87–19.37. Furthermore, the compounds showed no sign of cytotoxicity at the highest concentration tested (Table 2).

In order to evaluate the possibility of broad-spectrum antiviral activity of the newly identified inhibitors, compounds **1a-c** and **2b**, which inhibited SARS-CoV-2 replication were tested against the other highly-pathogenic betacoronavirus MERS-CoV, in VEROE6 cell line, and the alphacoronavirus HCoV229E, in BEAS2B cell line, using as control the protease inhibitor GC376 (Table 2). Results showed that all the compounds were active against MERS-CoV, with compounds **1a** and **1b** showing EC$_{50}$ values in the sub-micromolar range, while compounds **1c** and **2b** were active in the low micromolar range. A similar result was obtained against the replication of alphacoronavirus HCoV229E, tested

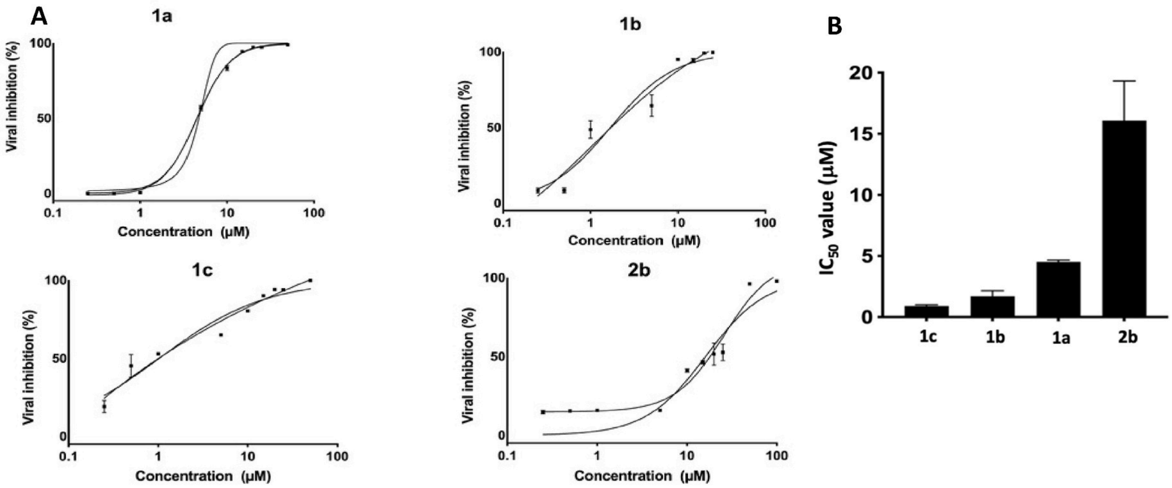

Fig. 3. Antiviral effect of DKAs inhibitors against SARS-CoV-2. (A) SARS-CoV-2 infected cells were treated with the compounds at concentrations ranging from 0.25 to 100 μM, and viral titer inhibition was calculated by plaque assay. Values are expressed as means ± the SD from three experiments, each performed in triplicate. (B) DKA inhibitors impair the infectivity of SARS-CoV-2 with different efficiencies as shown by the comparison among IC$_{50}$ values of the compounds.

Table 2
Inhibition of the replication of SARS-CoV-2, MERS-CoV and HCoV229E by DKAs.

Compound	SARS-CoV-2[a]EC$_{50}$ (μM)	MERS-CoV VEROE6[b]EC$_{50}$ (μM)	Vero E6[c]CC$_{50}$ (μM)	HCoV-229E BEAS2B[d]EC$_{50}$ (μM)	BEAS2B[e]CC$_{50}$ (μM)
1a	4.54 ± 0.15	0.33 ± 0.03	>264	0.54 ± 0.15	67.9 ± 7.3
1b	1.70 ± 0.45	0.76 ± 0.15	>264	0.91 ± 0.14	49.7 ± 3.8
1c	1.03 ± 0.24	6.32 ± 1.35	>264	1.83 ± 0.92	>100
2a	>30	ND	>264	ND	ND
2b	16.07 ± 3.25	5.18 ± 0.81	>264	3.39 ± 1.08	11.7 ± 1.2
2c	>30	ND	>264	ND	ND
GC376	0.018 ± 0.005	0.028 ± 0.003	>100	0.026 ± 0.012	>100

ND not done.

[a] SARS-CoV-2 Effective concentration 50·compound concentration required to reduce the SARS-CoV-2 replication in Vero cells by 50% concentration able to reduce the viral titer of 50%. Infected cells were treated with increasing concentrations, for 24 h and viral titer inhibition determined by plaque assay of the supernatant. Values are expressed as means ± the SD from two experiments, in triplicate.

[b] MERS-CoV Effective concentration 50, concentration able to reduce the viral titer of 50%. Infected cells were treated with increasing concentrations, for 24 h and viral titer inhibition determined by plaque assay of the supernatant. Values are expressed as means ± the SD from two experiments, in duplicate.

[c] compound concentration required to reduce Vero cells viability by 50%.

[d] HCoV 229E Effective concentration 50, concentration able to reduce the viral titer of 50%. Infected cells were treated with increasing concentrations of compound for 24 h and viral titer inhibition in the supernatant RT-qPCR. Values are expressed as means ± the SD from two experiments, in duplicate.

[e] Compound concentration required to reduce BEAS2B cells viability by 50%.

in BEAS2B cell line derived from the human bronchial epithelium. However, when tested against this last cell line, all compounds except **1c** exhibited higher cytotoxicity compared to VeroE6 cells. In particular compound **2b** showed a CC$_{50}$ of 11.7 μM.

The results showed a general trend of acidic derivatives being more potent than ester counterparts.

Compound **1b** and **1c**, characterized by the best inhibitory profile (considering both the enzymatic and cellular activities), was chosen for further characterization of its binding mode.

2.4. DKA binding mode prediction

A molecular docking protocol was applied to predict the possible binding mode of the DKA compounds on the nsp13 complex. The 3D model of the nsp13 helicase protein of SARS-CoV-2 adopted here is the SwissModel generated with the SARS-CoV helicase (PDB: 6JYT), already evaluated in a recent study by Perez-Lemus et al. (2022a). The mentioned complex reports the natural ligands: adenosine diphosphate (ADP) and single-stranded RNA (ssRNA). To predict which regions are involved in the binding of the DKA compounds, a binding site mapping procedure was carried out using GeneoNET* software finding two "druggable" binding sites in the 3D structure(Bocchi et al., 2022). The top-ranked binding site is the region comprehending ADP and RNA sites, with a druggability score of 0.82 (Yellow surface, Fig. 4). The second-ranked binding site is the allosteric site located in the RecA2 domain, druggability score of 0.79 (Red surface, Fig. 4).

2.5. Binging mode: experimental investigation

Since it was previously shown that for inhibitors that bind within the active site, e.g. of nucleic acid binding proteins, the competition with the natural substrate hampered an effective inhibition of the enzyme in the physiological context (Corona et al., 2020; Wang et al., 2020), we asked whether the time of addition of the nucleic acid in the reaction mixture could affect compounds potency of inhibition of the nsp13 unwinding assay, confirming the possible binding within the RNA binding site. To this aim, nsp13 unwinding inhibition by **1b and 1c** was measured pre-incubating the enzyme for 10 min either with the nucleic acid or the drug. Then the second component (drug or nucleic acid) was added, and the reaction was started by adding ATP (Fig. 5AB). Results showed that the inhibitors retained full potency against nsp13 unwinding if added before or after the substrate with IC$_{50}$ values of 4.2 ± 1.1 μM and 3.8 ± 1.1 μM respectively for 1b, and IC$_{50}$ values of 11.7 ± 2.8 μM and 10.5 ± 1.6 μM respectively for 1c. Similarly, also the NTPase activity was

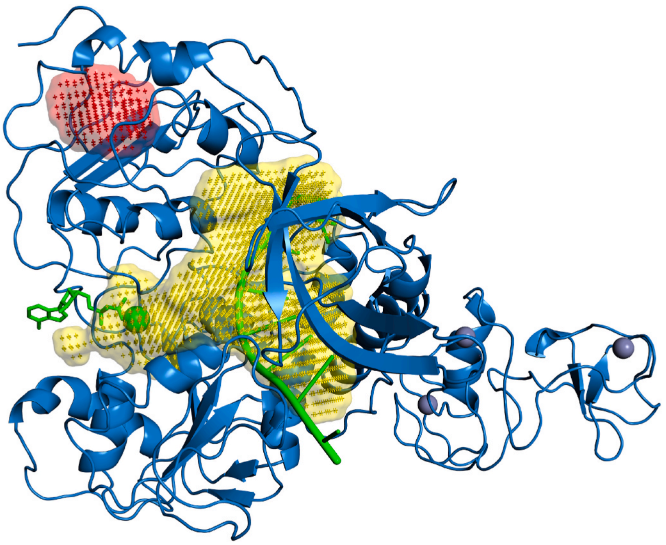

Fig. 4. Binding site prediction. The nsp13 structure is reported in blue cartoon and, for sake of clarity, ADP, magnesium and ssRNA are reported in green. The ADP and the 5′RNA binding site and the allosteric binding sites are reported in yellow and red surfaces respectively.

investigated in the presence of nucleic acid using a poly(A) ssRNA of 350 base pair, incubated for 10’ with the protein before compound addition. The results showed that the presence of PolyrA did not affect the potency of inhibition of **1b and 1c** vs the nsp13 ATPase activity if pre-incubated with the enzyme nor added to the reaction mix upon compound addition (1b IC_{50} = 12.7 ± 1.1 μM and 11.0 ± 1.2 μM respectively, 1c IC_{50} = 7.3 ± 0.6 μM and 10.9 ± 1.9 μM respectively) (Fig. 5DE).

Using the same experiment conditions, we also investigated the unwinding and the ATPase activity of the control SSYA10-001 in the presence of a nucleic acid or PolyrA. Results showed that the presence of the nucleic acid did not affect the potency of inhibition against the unwinding activity of SSYA10-001, with IC_{50} values of 4.06 ± 0.15 μM and 4.1 ± 0.9 μM, respectively (Fig. 6C). The same results were obtained for the potency of inhibition for ATPase activity of SSYA10-001, with IC_{50} values of 2.75 ± 0.5 μM and 2.2 ± 0.8 μM, respectively (Fig. 5F).

In order to determine the kinetics of inhibition by DKAs, and the possible contribution of the binding of the compound in the ATP binding site, both the nsp13-associated unwinding and ATPase activities were measured by titrating the ATP in the reaction mixture in the absence or presence of an increasing amount of **1b** (Fig. 6). Results showed that **1b** inhibited the unwinding activity acting non-competitively versus ATP (Fig. 6A), with a K_m value of 0,38 mM, consistent with what was previously reported that was only slightly affected by the presence of the inhibitor(Corona et al., 2022), while the Vmax showed a reduction proportional to the increase concentration of inhibitor, suggesting the profile of a possible mixed-type inhibition. Similarly, Results showed that **1b** inhibited also the ATPase activity acting non-competitively versus ATP (Fig. 6B). These results suggest a binding of DKAs outside of the ATP binding site, and support the hypothesis of binding into the allosteric pocket in the RecA2 domain.

To better investigated the suggested binding to the RecA2 domain and its similarity with SSYA10-001 for the binding pose, we investigated the effect of the simultaneous presence of SSYA10-001 and **1b** in the reaction mixture in the nsp13 unwinding assay (Fig. 6C). Results were plotted as IC_{50} value of SSYA10-001 as a function of increasing concentrations of **1b**. The resulting isobologram showed that the two compounds have a purely additive effect on the inhibition of nsp13 unwinding activity. The data is not in contradiction with the same binding site prediction. To further explore this possibility we performed a Yonetani-Theorell analysis of the combination of SSYA10-001 and compound **1b** on nsp13 unwinding activity. This model allows to discriminate between inhibitors that are kinetically mutually exclusive (potentially competing for a single binding site) and inhibitors that are kinetically not mutually exclusive (potentially binding to non-overlapping sites) (Yonetani et al., 1982). Results showed that the binding of compound **1b** is kinetically mutually exclusive with SSYA10-001, in agreement with the same binding site prediction by molecular modelling (Fig. 6D).

2.6. *Docking prediction of DKA binding within nsp13 RecA2 domain*

Following the indication of the binding within the RecA2 domain as the most supported by experimental results, we performed a molecular docking using LiGen in this allosteric binding site to predict the binding mode of the best-acting compound **1b** and of its *N*-allyl analog **1a** (Manelfi et al., 2021), in comparison with the reference molecule SSYA10-001 (Fig. 7), and to hypothesize the key residues of the RecA2

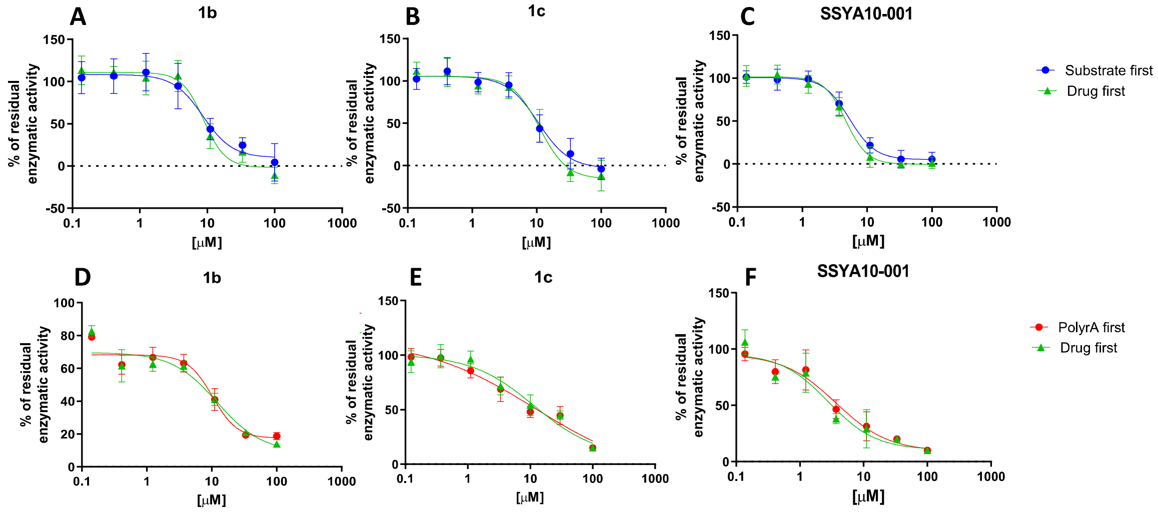

Fig. 5. Impact of time of addition of nucleic acid on compounds activity: [A-C] Inhibition of the nsp13-associated unwinding activity by DKA **1b**, **1c** and **SSYA10-001**pre-incubating nsp13 for 10 min with the dsDNA substrate (blue line) or compound (green line); [D-F] inhibition of the nsp13-associated ATPase activity by DKA **1b, 1c** and **SSYA10-001**pre-incubating nsp13 for 10 min with the polyrA (red line) or with the inhibitor (green line). Values are expressed as means ± the SD from two experiments, in triplicate.

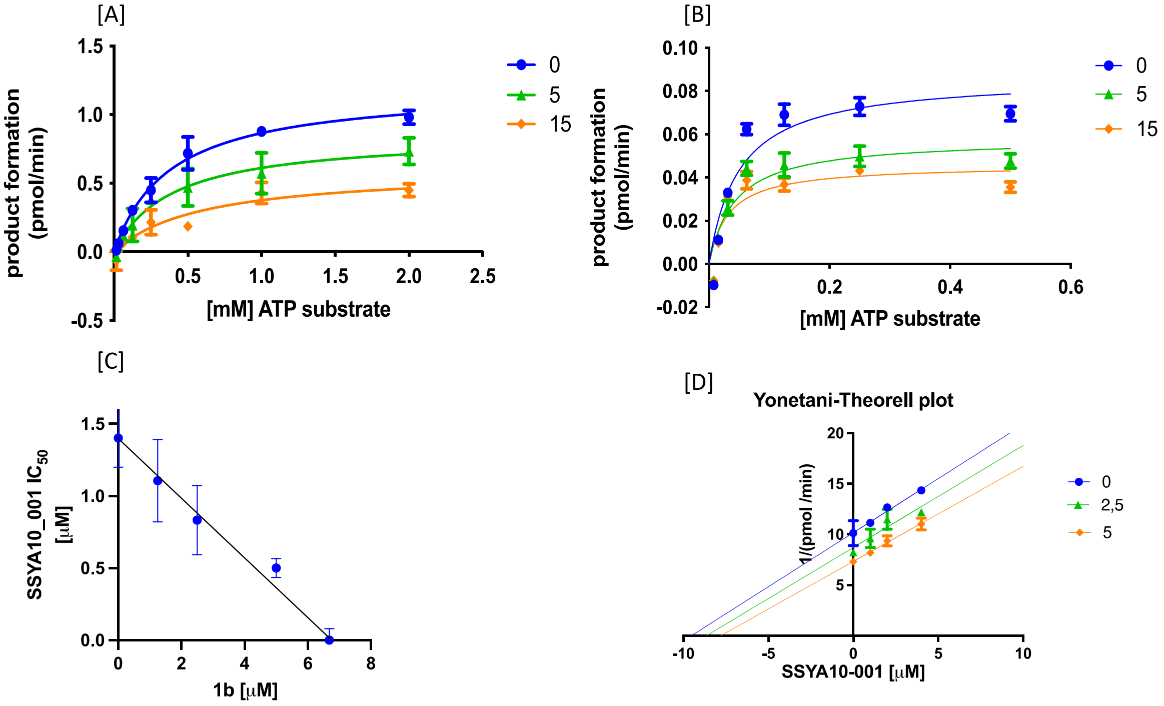

Fig. 6. Kinetics of inhibition of nsp13-associated activities by DKA 1b [A] kinetics of the nsp13-associated unwinding activity in absence (blue line) or presence of **1b** 5 μM (green line) 15 μM (orange line) **[B]** kinetics of the nsp13-associated NTPase activity in the absence (blue line) or presence of **1b** 5 μM (green line) 15 μM (orange line) **[C] Isobologram analysis** of reciprocal effect of SSYA10-001and compound **1b** on nsp13 unwinding activity. **[D] Yonetani-Theorell analysis.** Combination of SSYA10-001 and compound **1b** on nsp13 unwinding activity. 1/pmol of reaction product as function of SSYA10-001 concentration in absence (blue line) or presence of **1b** 2.5 μM (green line) or 5 μM (orange line). Values are expressed as means ± the SD from two experiments, in triplicate.

domain involved in the interactions with the inhibitors.

All the compounds showed a similar binding mode in this pocket sharing common interactions with some key residues (Arg507, Phe511, Asn503). In particular, the hydrophobic portion of compounds **1b** and **1a** lies in a hydrophobic channel of the pocket, with the aromatic ring and the alkene chain substituents of the indole nitrogen enclosed by the

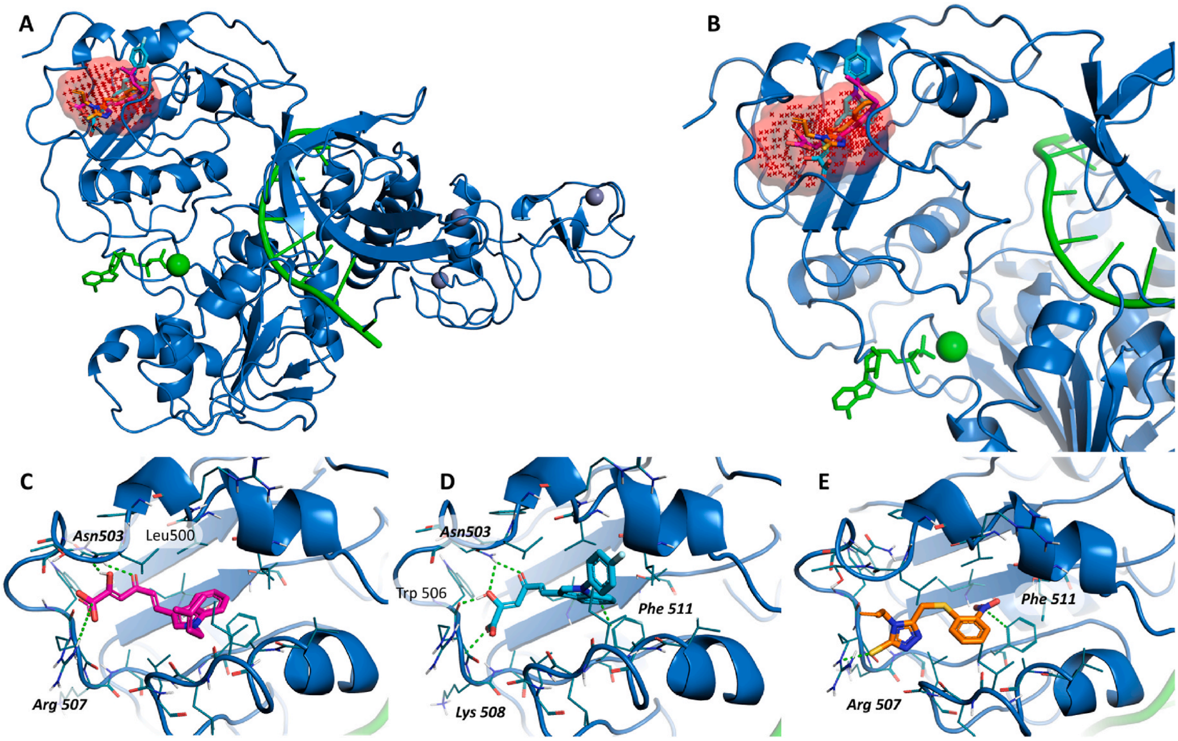

Fig. 7. A-B: Overlapping binding poses of compounds 1a (pink), 1b (light blue) and SSYA10-001 (orange) in the RecA2 domain. C-D-E: Zoom on the binding mode of each molecule, showing the residues involved in the key interactions.

side chains of residues Ala522, Ile 493, Ile525 and Leu500, and the indole ring showing pi stacking with Phe511. Also, the aromatic ring of the reference molecule SSYA10-001 lies in the same cavity showing similar interactions. On the other hand, the DKA portion of compounds **1a** and **1b** shows H bond interactions with the side chains of the residues Asn503 and Arg507 and the backbone of Lys508 and Trp506. According to what was previously reported, the reference molecule also SSYA10-001 interacts with the residue Arg507 (Perez-Lemus et al., 2022b).

3. Discussion

For RNA viruses, RNA helicases have long been recognized to play critical roles during virus replication cycles, facilitating proper folding and replication of viral RNAs, thus representing promising druggable targets for the development of new drugs (Kwong et al., 2005). Moreover, given that SARS-CoV-2 nsp13 is a highly conserved protein among all known coronaviruses (Spratt et al., 2021), recently explored by fragment-based approach to identify new possible small-molecules binding sites (Newman et al., 2021), it can be postulated that nsp13 may represent a promising target for the development of antiviral agents and that compounds binding in the pockets near conserved motifs may serve as broad-spectrum antiviral agents. Following the first report of DKAs as enzymatic inhibitors of SARS-CoV-1 nsp13 (Lee et al., 2009) and exploiting the high degree of sequence identity between SARS-CoV-1 and SARS-CoV-2 nsp13 enzymes, we report an in-depth analysis of the anti-nsp13 activity of a set of DKA derivatives. Among the six DKAs here reported, all were able to block both nsp13 enzymatic activities with higher potencies than that of the ATPase inhibitor licoflavone C. Moreover, about all compounds were active against unwinding in the same order of magnitude of the helicase inhibitor SSYA10-001, firstly reported against SARS-CoV (Adedeji et al., 2014), sharing with the same compound also the proposed binding mode within the allosteric RecA2 site previously suggested by Perez-Lemus et al. (2022a) as the binding site for bananine derivates. Noteworthy, RecA2 has been recently reported to play a very dynamic role in SARS-CoV-2 RTC-activity (Chen et al., 2022b) The site shows residues that are conserved among all hCoVs (Adedeji et al., 2014), suggesting possibilities for broad-spectrum inhibitory activities.

Among the tested compounds, **1a-c** and **2b** were able to inhibit SARS-CoV-2 replication in the low micromolar/submicromolar range without exerting cytotoxicity at the tested concentration. Compound **1b** proved to be characterized by the best inhibitory profile (considering both the enzymatic and cellular activities), while the best acting against infected cells was derivative **1c**, showing an antiviral activity of 1.03 μM. It is also worthy of note that this compound proved to be endowed with the best antiviral activity among the nsp13 inhibitors reported so far, e.g., the unwinding inhibitor SSYA10-001 (IC_{50} of 85 μM) (Zeng et al., 2021) or the dual nsp13 inhibitor licoflavone C that was inactive in cell-based assays up to 100 μM (Corona et al., 2022). Its activity, though, is comparable only with the drug clofazimine, recently described as a SARS-CoV-2 inhibitor able to block also nsp13 unwinding activity with an IC_{50} around 7 μM and to block SARS-CoV-2 replication in Vero E6 cells with an IC_{50} equal to 0.31 μM (Yuan et al., 2021). Further investigations were performed with compounds **1a-c** and **2b** against other HCoVs, to evaluate the spectrum of inhibition. MERS-CoV and the alpha coronavirus HCoV 229E were both inhibited by the tested compounds, hence proving a retained antiviral activity.

The compound binding hypothesis, provided by molecular docking, suggested the possibility of binding within the ADP and RNA sites and within the RecA2 domain. Since as previously reported, the competition with the substrate hampers an effective inhibition of the enzyme in the physiological context (Corona et al., 2020; Wang et al., 2020), such hypothesis was investigated by competition-assays with the natural ligands of ADP and RNA binding sites. Compounds proved to be not competitive with ATP and to not be affected in their potency of inhibition by the preliminary presence of oligos and not to halter the K_m value of ATP in kinetic evaluation, supporting the hypothesis of binding within the second predicted binding site, in the RecA2 domain, the same reported for reference molecule **SSYA10-001** (Perez-Lemus et al., 2022b). Such a hypothesis was investigated by Isobologram and Yonetani-Theorell analysis, which support a same-site binding hypothesis by kinetically mutually-exclusive behavior, and pure additive effect, observed for the simultaneous presence of **SSYA10-001** and **1b** in the enzymatic assay. At last a docking prediction of the DKA binding mode within this pocket was performed, to acquire some insight to guide the future design of DKA analogues. Possible interactions were suggested of compound **1b** with residues previously described as significant for the binding of compound **SSYA10-001** (Perez-Lemus et al., 2022b).

Overall, the activity of compound **1b** against nsp13 function and against viral replication proved to be highly promising, paving the way for the development of new nsp13 inhibitors. Further studies are needed to evaluate the ADMET properties of this new class of compounds in order to deepen the role of the DKA branch. Indeed, it is widely reported that this group is biologically liable due to high metabolic turnover and because it shows poor cell membrane penetration. Furthermore, it has been proven to have a time-dependent decrease in the activity in solutions at room temperature, even during short periods of time (Krieger et al., 2012). For this reason, a variety of compounds were developed by mimicking the DKA element into scaffolds characterized by improved drug-like qualities, thus overcoming the biological liability of the DKA moiety. Several examples have been reported in the literature, such as in the case of anti-HIV agents (Summa et al., 2008; Zeng et al., 2008). We also reported an isosteric approach to overcome the DKA liabilities for the development of several antiretroviral agents (Messore et al., 2020, 2021).Taking advantage of this knowledge, future steps in this research will explore these approaches, thus moving forward from hit-to-lead development.

4. Conclusions

In this work, we described a new series of compounds as inhibitors of both the nsp13-associated activities, active against SARS-CoV-2 replication in cell-based assays. Among the tested compounds, compound **1b** showed the best inhibitory profile (considering both the enzymatic and cellular activities). It proved to inhibit both the unwinding and ATPase activities in the low micromolar range, being more potent than licoflavone C *vs* the unwinding and ATPase (more than 1.5-fold and about 3-fold, respectively), even though less potent than SSYA10-001 *vs* helicase. Moreover, in silico studies suggested an allosteric binding mode, in agreement with its kinetics of inhibition. Indeed, **1b** inhibited the unwinding and the ATPase activities acting non-competitively versus ATP. It is also worthy of note that the antiviral activity of compound **1b** is comparable with the most potent anti-SARS-CoV-2 agents described in literature tested against infected Vero E6 cells and active against different enzymatic targets.

Taken together, these data highlight the importance of this new class of nsp13 inhibitors. Indeed, to the best of our knowledge, they represent the first report of inhibitors active against both the SARS-CoV-2 nsp13-associated activities and capable also of blocking viral replication in SARS-CoV-2 infected cells. Even though further investigation will be needed to study the structure-activity relationships of this new class of nsp13 inhibitors, the experimental results described herein give important insights for a future hit-to-lead optimization aiming at designing new analogues with improved inhibitory profiles.

5. Materials and methods

5.1. Chemistry

General. Melting points were determined on a Bobby 555 Stuart Scientific SMP1 melting point apparatus and are uncorrected. Compound purity was always >95% as determined by combustion analysis.

Analytical results agreed to within ±0.40% of the theoretical values. IR spectra were recorded on a PerkinElmer Spectrum-One spectrophotometer. ^{1}H NMR spectra were recorded at 400 MHz on a Bruker AC 400 Ultrashield 10 spectrophotometer (400 MHz). Deuterochloroform 98.8% (CAS 865−49−6) of isotopic purity (Aldrich) was used. Column chromatographies were performed on silica gel (Merck; 70−230 mesh). All compounds were routinely checked on thin-layer chromatography (TLC) using aluminum-baked silica gel plates (Fluka DC-Alufolien Kieselgel 60 F_{254}). Developed plates were visualized by UV light. Solvents were of reagent grade and, when necessary, were purified and dried by standard methods. Concentration of solutions after reactions and extractions involved the use of a rotary evaporator (Büchi) operating at a reduced pressure (ca. 20 Torr). Organic solutions were dried over anhydrous sodium sulfate (Merck). All solvents were freshly distilled under nitrogen and stored over molecular sieves for at least 3 h prior to use. Analytical results agreed to within ±0.40% of the theoretical values.

5.1.1. General experimental procedures

General Procedure A (GP-A) to Obtain Enone Derivatives ***3a,b***. A mixture of the proper aldehyde **4a,b** (0.02 mol) in 70 mL of acetone and 5 N NaOH (30 mL) was stirred at room temperature (for derivative **3a**) or at 50 °C (for derivative **3b**) for 3 h (for derivative **3a**) or for 72 h (for derivative **3b**). Afterwards, water was added and the mixture was neutralized with 1 N HCl. For derivative **3a**, ethyl acetate (250 mL) was added, the organic fractions were combined, washed with water (2 × 100 mL), with saturated NaCl solution (200 mL), dried over sodium sulfate, filtered and evaporated under reduced pressure. The so obtained raw was purified by column chromatography (SiO_2) using *n*-hexane/ethyl acetate 2:1 as eluent, affording **3a** as a yellow wax. For derivative **3b**, the crude was treated with water (90 mL) and the resulting solid was filtered, washed with water (2 × 50 mL), petroleum ether and dried under IR lamp to afford **3b** as an orange solid. For each compound recrystallization solvent; yield (%); melting point (°C); IR; ^{1}H NMR and elemental analysis are reported.

General Procedure B (GP-B) to Obtain Diketo Ester Derivatives ***2a,b***. Freshly prepared sodium ethoxide, obtained by the dissolution of Na (0.032 mol) in 22 mL of absolute ethanol, was added to a solution of the proper enone derivative **3a,b** (0.016 mol) and diethyl oxalate (0.032 mol) in anhydrous THF (17 mL) under argon atmosphere. The mixture was stirred at room temperature for 1.5 h and then was poured into *n*-hexane (260 mL). The collected precipitate was vigorously stirred for 30 min in 1 N HCl (260 mL). The solid that formed was filtered, washed with water and petroleum ether, and dried under IR lamp to afford the pure diketo esters. For each compound recrystallization solvent; yield (%); melting point (°C); IR; ^{1}H NMR and elemental analysis are reported.

General Procedure C (GP-C) to Obtain Diketo Acid Derivatives ***1a,b***. A mixture of 1 N NaOH (28 mL) and the appropriate ester **2a,b** (0.06 mol) in 1:1 THF/MeOH (28 mL) was stirred at room temperature for 1.5 h. The mixture was poured into crushed ice and then treated with 1 N HCl until pH 3 was reached. For derivative **1a**, ethyl acetate (200 mL) was added, the organic fractions were combined, washed with water (2 × 100 mL), with saturated NaCl solution (150 mL), dried over sodium sulfate, filtered and evaporated under reduced pressure, obtaining a red solid as pure product. For derivative **1b**, the resulting solid was filtered, washed with water (2 × 50 mL), petroleum ether and dried under IR lamp to afford **1b** as a red solid. For each compound recrystallization solvent; yield (%); melting point (°C); IR; ^{1}H NMR and elemental analysis are reported.

5.1.1.1. Synthesis of 1-(3-methylbut-2-en-1-yl)-1H-indole-3-carbaldehyde (4a). To a solution of 1*H*-indole-3-carboxaldehyde (4 g, 0.03 mol) in anhydrous DMF (59 mL), NaH (2.16 g, 0.09 mol) was added in small portion within 10 min at room temperature. After development of H_2, the solution was treated with 3,3-dimethylallyl bromide 4.77 g, 0.03 mol) and the resulting mixture was stirred at room temperature for 1 h. The mixture was poured into crushed ice and the resulting solid was filtered, washed with water (2 × 50 mL), petroleum ether and dried under IR lamp to afford **4a** as a pink solid (5.24 g, 89% yield). Recrystallization solvent: cyclohexane; mp 95 °C; IR ν 1648 (C═O) cm^{-1}; ^{1}H NMR ($CDCl_3$) δ 1.70 (s, 3H, CH_3), 1.82 (s, 3H, CH_3), 4.89 (d, 2H, CH_2), 5.70–5.74 (m, 1H, CH═C), 7.33 (m, 2H, indole C5–H and C6–H), 7.63 (dd, 1H, indole C7–H), 8.15 (dd, 1H, indole C4–H), 8.33 (s, 1H, indole C2–H), 9.95 (s, 1H, aldehyde CH). Anal. calcd for $C_{14}H_{15}NO$: C, 78.84; H, 7.09; N, 6.57%. Found: C, 78.79; H, 7.05; N, 6.56%.

5.1.1.2. Synthesis of 1-(4-fluorophenyl)-1H-indole-3-carbaldehyde (4b). 1*H*-indole-3-carboxaldehyde (0.7 g, 0.0048 mol), cupric acetate (2.19 g, 0.012 mol), 4-fluorophenylboronic acid (1.18 g, 0.0084 mol), and 1:1 NMP/pyridine mixture (7.2 mL) were placed in a 100 mL round-bottom flask. The bottom part of the flask was placed into the microwave cavity (60 W, 120 °C, 50 s, open vessel). The microwave irradiation was repeated six times, and after each cycle, the mixture was cooled and cupric acetate (0.012 mol), phenylboronic acid (0.0084 mol), and NMP/pyridine mixture (7.2 mL) were added. After a final cycle of 15 min, the mixture was cooled, diluted with THF and filtered off and the solvent was evaporated. The residue was dissolved in ethyl acetate, washed with 1 N HCl (15 times) and saturated NaCl solution (three times), and dried, and the solvent was evaporated under reduced pressure. The crude product was purified by column chromatography (SiO_2) using *n*-hexane/ethyl acetate 1:1 as eluent, affording **4b** as a brown solid (0.68 g, 48% yield). Recrystallization solvent: cyclohexane; mp 158 °C; IR ν 1652 (C═O) cm^{-1}; ^{1}H NMR ($CDCl_3$) δ 7.36 (d, 2H, benzene H), 7.55 (d, 1H, indole C7–H), 7.69–7.74 (m, 4H, indole C5–H, C6– H and benzene H), 8.21 (m, 1H, indole C4–H), 8.60 (s, 1H, indole C2–H), 10.04 (s, 1H, aldehyde CH). Anal. calcd for $C_{15}H_{10}FNO$: C, 75.30; H, 4.21; F, 7.94; N, 5.85%. Found: C, 75.27; H, 4.22; F, 7.93; N, 5.86%.

5.1.1.3. (E)-4-(1-(3-methylbut-2-en-1-yl)-1H-indol-3-yl)but-3-en-2-one (3a). Compound **3a** was prepared from **4a** by means of GP-A. Cyclohexane; 83% as a yellow wax; 53 °C; IR ν 1656 (C═O) cm^{-1}; ^{1}H NMR ($CDCl_3$) δ 1.65 (s, 3H, CH_3), 1.72 (s, 3H, CH_3) 2.29 (s, 3H, butenoate C1–H), 4.77 (d, 2H, CH_2), 5.66–5.68 (m, 1H, $\mathit{CH}{=}C(CH_3)_2$), 6.69 (d, 1H, Jt = 16 Hz, butenoate C3–H), 7.20–7.26 (m, 3H, indole C5–H, C6–H and C7–H), 7.54 (d, 1H, indole C4–H), 7.80 (d, 1H, Jt = 16 Hz, butenoate C4–H), 7.94 (s, 1H, indole C2–H). Anal. calcd for $C_{17}H_{19}NO$: C, 80.60; H, 7.56; N, 5.53%. Found: C, 80.57; H, 7.55; N, 5.52%.

5.1.1.4. (E)-4-(1-(4-fluorophenyl)-1H-indol-3-yl)but-3-en-2-one (3b). Compound **3b** was prepared from **4b** by means of GP-A. Benzene; 51% as an orange solid; 149 °C; IR ν 1655 (C═O) cm^{-1}; ^{1}H NMR ($CDCl_3$) δ 2.38 (s, 3H, butenoate C1–H), 6.86 (br d, 1H, butenoate C3–H), 7.37 (d, 2H, benzene H), 7.52 (d, 1H, indole C7–H), 7.67–7.73 (m, 4H, indole C5–H, C6–H and benzene H), 7.88 (br d, 1H, butenoate C4–H), 8.01 (m, 1H, indole C4–H), 8.36 (s, 1H, indole C2–H). Anal. calcd for $C_{18}H_{14}FNO$: C, 77.40; H, 5.05; F, 6.80; N, 5.01%. Found: C, 77.42; H, 5.05; F, 6.81; N, 5.01%.

5.1.1.5. Ethyl (2Z,5E)-2-hydroxy-6-(1-(3-methylbut-2-en-1-yl)-1H-indol-3-yl)-4-oxohexa-2,5-dienoate (2a). Compound **2a** was prepared from **3a** by means of GP-B. Cyclohexane; 75% as a yellow solid; 102 °C; IR ν 3451 (OH), 1728 (C═O ester), 1677 (C═O ketone) cm^{-1}; ^{1}H NMR ($CDCl_3$) δ 1.40 (t, 3H, $OCH_2\mathit{CH_3}$), 1.81 (s, 3H, CH_3), 1.84 (s, 3H, CH_3), 4.37 (q, 2H, $O\mathit{CH_2}CH_3$), 4.71 (d, 2H, CH_2), 5.38–5.41 (m, 1H, $\mathit{CH}{=}C(CH_3)_2$), 6.53 (s, 1H, hexenoate C3–H), 6.65 (d, 1H, Jt = 16 Hz, hexenoate C5–H), 7.28–7.35 (m, 2H, indole C5–H and C6–H), 7.39 (d, 1H, indole C7–H), 7.51 (s, 1H, indole C2–H), 7.93 (d, 1H, indole C4–H), 8.01 (d, 1H, Jt = 16 Hz, hexenoate C6–H). Anal. calcd for $C_{21}H_{23}NO_4$: C, 71.37; H, 6.56; N, 3.96%. Found: C, 71.35; H, 6.55; N, 3.96%.

5.1.1.6. Ethyl (2Z,5E)-6-(1-(4-fluorophenyl)-1H-indol-3-yl)-2-hydroxy-4-oxohexa-2,5-dienoate (2b). Compound **2b** was prepared from **3b** by means of GP-B. Isopropyl ether; 82% as an orange solid; 154 °C; IR ν 3535 (OH), 1736 (C═O ester), 1676 (C═O ketone) cm^{-1}; ^1H NMR ($CDCl_3$) δ 1.43 (t, 3H, OCH_2CH_3), 4.40 (q, 2H, OCH_2CH_3), 6.57 (d, 1H, hexenoate C3–H), 6.77 (d, 1H, Jt = 16 Hz, hexenoate C5–H), 7.30 (d, 2H, benzene H), 7.34–7.38 (m, 2H, benzene H), 7.45–7.51 (m, 3H, indole C5–H, C6–H and C7–H), 7.66 (s, 1H, indole C2–H), 8.01 (d, 1H, indole C4–H), 8.05 (d, 1H, Jt = 16 Hz, hexenoate C6–H). Anal. calcd for $C_{22}H_{18}FNO_4$: C, 69.65; H, 4.78; F, 5.01; N, 3.69%. Found: C, 69.64; H, 4.78; F, 5.00; N, 3.69%.

5.1.1.7. Ethyl (2Z,5E)-6-(1-benzyl-1H-indol-3-yl)-2-hydroxy-4-oxohexa-2,5-dienoate (2c). Synthesis, analytical, and spectroscopic data are reported in literature (Costi et al., 2013a)

5.1.1.8. (2Z,5E)-2-hydroxy-6-(1-(3-methylbut-2-en-1-yl)-1H-indol-3-yl)-4-oxohexa-2,5-dienoic acid (1a). Compound **1a** was prepared from **2a** by means of GP-C. Washed with boiling EtOH; 70% as a red solid; 137 °C; IR ν 3281 (OH), 1754 (C═O acid), 1617 (C═O ketone) cm^{-1}; ^1H NMR ($CDCl_3$) δ 1.82 (s, 3H, CH_3), 1.84 (s, 3H, CH_3), 4.71 (d, 2H, CH_2), 5.38–5.41 (m, 1H, $CH{=}C(CH_3)_2$), 6.59 (s, 1H, hexenoate C3–H), 6.61 (d, 1H, Jt = 16 Hz, hexenoate C5–H), 7.33–7.39 (m, 2H, indole C5–H, C6–H and C7–H), 7.54 (s, 1H, indole C2–H), 7.92 (d, 1H, indole C4–H), 8.05 (d, 1H, Jt = 16 Hz, hexenoate C6–H). Anal. calcd for $C_{19}H_{19}NO_4$: C, 70.14; H, 5.89; N, 4.31%. Found C, 70.12; H, 5.88; N, 4.31%.

5.1.1.9. (2Z,5E)-6-(1-(4-fluorophenyl)-1H-indol-3-yl)-2-hydroxy-4-oxohexa-2,5-dienoic acid (1b). Compound **1b** was prepared from **2b** by means of GP-C. Washed with isopropanol; 54% as a red solid; 174 °C; IR ν 3530 (OH), 1707 (C═O acid), 1673 (C═O ketone) cm^{-1}; ^1H NMR ($CDCl_3$) δ 6.63 (d, 1H, hexenoate C3–H), 6.71 (d, 1H, Jt = 16 Hz, hexenoate C5–H), 7.27–7.33 (m, 2H, benzene H), 7.34–7.38 (m, 2H, benzene H), 7.44–7.50 (m, 3H, indole C5–H, C6–H and C7–H), 7.68 (s, 1H, indole C2–H), 8.00 (d, 1H, indole C4–H), 8.10 (d, 1H, Jt = 16 Hz, hexenoate C6–H). Anal. calcd for $C_{20}H_{14}FNO_4$: C, 68.37; H, 4.02; F, 5.41; N, 3.99%. Found: C, 68.35; H, 4.02; F, 5.40; N, 3.99%.

5.1.1.10. (2Z,5E)-6-(1-benzyl-1H-indol-3-yl)-2-hydroxy-4-oxohexa-2,5-dienoic acid (1c). Synthesis, analytical, and spectroscopic data are reported in literature (Costi et al., 2013a)

5.2. Virus production

A virus working stock was prepared through the propagation in Vero cells cultured in minimum essential medium (MEM) containing 2% (w/v) fetal bovine serum (Euroclone S.p.A.) of a strain of SARS-CoV-2 (hCoV-19/Italy/CDG1/2020/EPI_ISL_412,973), isolated from a nasopharyngeal swab by Department of Infectious Diseases, National Institute of Health Rome, Italy. The culture supernatants of infected Vero cells, collected after 72 h from the infection, were clarified through centrifugation at 600*g* for 5 min. The concentration of infectious virus was determined by plaque-forming assay.

Middle East respiratory syndrome (MERS) Coronavirus, strain IP/COV/MERS/Hu/France/FRA2 (Ref-SKU: 014V-02970) was provided by EVA-GLOBAL Jessica VANHOMWEGEN laboratory, Pasteur Institute. A virus working stock was prepared through the propagation in Vero cells cultured in DMEM (gibco) + 1% FBS Heat Inactivated (gibco). On day 1, 1*10ˆ5 cells/ml were seeded and on the second day, washed with PBS and infected with MERS-CoV at m.o.i. of 0.02 in media without FBS in one volume 1 ml for 1,5 h, after, 10 ml of maintenance media were added +1% FBS HI+1%PS. The stock was recovered 4 days after infection when a clear cytopathic effect was visible. The virus was clarified by centrifugation at 3000*g* X 20′and single-use aliquots were stored at −80 °C. The virus was titrated by plaque assay.

hCoV229E (ATCC® VR-740™) was in propagated in MRC-5 cells (ATCC:CCL-171™) maintained in MEM (Gibco) supplemented with 10% v/v fetal beef serum (FBS HI; Gibco), 1 mM Na Pyruvate (Euroclone), 1 mM Non Essential Amino Acids (Euroclone) and 1x Pen-strep (Euroclone) and kept under 5% CO_2 on 35 °C. On day 1, 1*10ˆ5 cells/ml were seeded and on the second day, washed with PBS and infected with HCoV229E with a m.o.i. of 0.05 in 1 ml for 2 h. After, 10 ml of maintenance media were added +2% FBS HI. Cells were visually inspected for viral-induced cytopathic effect and 3 days post-infection virus was clarified by centrifugation at 4000*g* X 5′and single-use aliquots were stored at −80 °C. The virus was titrated by CPE TD_{50} determination.

Virus isolation and virus propagation assay of SARS-CoV-2 and MERS-CoV needs to be conducted in a bio-safety Level-3 facility according to WHO laboratory biosafety guidance.

5.3. Cellular toxicity assay

The cellular toxicity of the compounds was evaluated by a trypan blue (0.02% final concentration) exclusion assay. Briefly, Vero E6 monolayers were incubated with different concentrations of compounds starting from the highest concentration of 264 μ**M** for 24, 48 and 72 h, respectively. Because the substances were dissolved in DMSO (percentage 0,25 to 5%), cellular toxicity of compounds was compared to that obtained by DMSO treatment, to determine if any changes observed were due to the DMSO or if they are due to the compounds.

The cellular toxicity of the compounds in Beas-2B cells was evaluated by MTT assay. Beas-2B cells were maintained in DMEM/F-12 (Gibco), 5% FBS HI (Gibco), 1% Kanamycin (Thermo-Fisher Scientifics), at 37 °C with 5% CO2. On day one, $2*10^4$ cells per well, 100 μl, are seeded in transparent 96 well plate and incubated over night to allow attachment and cell growth in order to reach 90% confluency. On day two, the culture medium is replaced with compound dilutions in DMEM/F-12. For untreated controls the culture medium is replaced with DMEM/F-12 with 0,1% DMSO. The cells were incubated for 24 h at 35 °C with 5% CO_2. After, 20 μl of 3-(4,5-dimethylthiazol-2-yl)-2,5-diphenyl-2H-tetrazolium bromide (Sigma-Aldrich) dissolved in PBS at 7,5 mg/ml in, were added to each well, the cells were incubated at 37 °C with 5% CO_2 for 1h. Then the supernatant was removed and cells lysed with 100 μl/well of: 100% 2-Propanol, 0,004% Triton-X-100 (Sigma-Aldrich), 0,0004% Hydrogen Chloride until the formazan crystals are completely dissolved, then the absorbance is read at 570 nm with a plate reader (Nivo-Viktor III)

5.4. SARS CoV-2 plaque assay

Vero-E6 cells monolayer was infected for 1 h at 37 °C with SARS-CoV-2 (0.01 MOI); after 1 h incubation, the medium was removed and replaced with fresh medium supplemented with 2% FBS and containing respectively each indole derivative at different concentrations. Untreated-infected cells were used as positive control of viral infection. After 24 h, the supernatants were collected and used to infect Vero E6 cells seeded in a 12/24-well plate for 1 h at 37 °C. After viral adsorption period, the inoculum was removed and the cell monolayer was overlaid with a mixture of MEM (no glutamine, no phenol-red-GIBCO), 1.5% Tragacanth (SIGMA), $NaHCO_3$ 7% (Gibco), L-glutamine 1X (Gibco), MEM NEAA 1x (Gibco), 0.02 M Hepes (Euroclone), DMSO (Sigma-Aldrich) and 2% FBS (final concentration). To calculate PFU, five days post-infection the mixture was removed carefully, plates were washed with saline solution and stained with 1% crystal violet for 20 min. The plaque reduction ratio was used to determine the rate of inhibition and calculated as (100-N/N0x100), where N is the PFU count of the treated sample, and N0 is the PFU count of the control sample. The plaque assay was also used to determine the concentration of molecules that inhibits 50% of viral titer in each well (IC_{50}).

The IC_{50} value was also determined and graphed by GraphPad Prism v9.0 software by fitting a variable slope-sigmoidal dose-response curve.

5.5. MERS CoV plaque assay

Cells were seeded at 10000 cells/well in 96-well black cell-treated plates. The following day, cells were incubated with the control compounds at different concentrations and the virus at MOI 0.005. GC376 compound Kuzikov et al. (2021) was used as positive control, in presence of 2 mM Pgp inhibitor CP-100356 (Hu et al., 2021). After 24 h, the supernatants were collected. Supernatant serial dilutions were made in DMEM 2%FBS, 0.075% Sodium Bicarbonate, and used to infect Vero E6 cells seeded in a 24-well plate in 200 μl of (200 000 cells/well) for 1,5 h at 37 °C. After that the medium containing virus was removed and cells were overlayed with 400 μl of DMEM 2%FBS +1% methyl cellulose 0.075% Sodium Bicarbonate and plates were incubated at 37 °C 5% CO_2 for 4 days.

To determine the PFU/ml, the mixture was removed carefully, plates were washed with PBS, and fixed with 300 μl of 4% PFA solution in PBS for 120 min. Then the monolayer was stained with 1% crystal violet solution in 10% Ethanol for 15 min.

The plaque reduction ratio was used to determine the rate of inhibition and calculated as (100-N/N0x100), where N is the PFU count of the treated sample, and N0 is the PFU count of the control sample. The plaque assay was also used to determine the concentration of molecules that inhibits 50% of viral titer in each well (EC_{50}).The EC_{50} value was also determined and graphed by GraphPad Prism v9.0 software by fitting a variable slope-sigmoidal dose-response curve.

5.6. hCoV229E replication assay

BEAS-2B cells were kindly provided by Pierre-Olivier Vidalain were maintained in DMEM/F-12 (Gibco), 5% FBS HI (Gibco), 1% Kanamycin (Thermo-Fisher Scientifics), at 37 °C with 5% CO_2. $2*10^4$ cells per well were seeded in transparent 96 well plate and incubated overnight in order to reach 90% confluency. 24h later cells were infected with hCoV-229E m.o.i. 0.06 in DMEM/F-12 in presence of compound or 0,1% DMSO (untreated controls). The cells were incubated for 2 h at 35 °C with 5% CO_2, then the virus was removed, replaced with complete medium with or without compound, and incubated at 35 °C with 5% CO_2. After 24h cells were lysed in RLT buffer and RNA extraction was performed using Tryzol (Thermo-Fisher Scientifics) as per manufacture instruction. The quantification of the viral RNA was evaluated through RT-qPCR using a Luna Universal One Step Kit (New England Biolabs) as HCoV229E-N gene copy number normalized to the constitutively expressed gene GAPDH. Primers used: N HCoV 229E Forward 5′-CGTCAGGGTAGAATACCTT-3’; N HCoV 229E Reverse 5′-CCTGTGCCAAGATAATAAAAATGC-3′, GAPDH Forward 5′-GAGT-CAACGGATTTTGGTCGT-3′, GAPDH Reverse 5′-TTGATTTTGGAGG-GATCTCG-3’.

5.7. SARS-CoV-2 nsp13 expression and purification

SARS-CoV-2 nsp13 was expressed from pNIC-ZB vector (addgene 159614) (Newman et al., 2021) with an adapted protocol. Briefly, the plasmid was transformed into E. coli BL21 Rosetta 2 cells. Cell cultures were grown in Terrific Broth media at 37 °C at 200 rpm. When the OD600 reached 1.6 expression was induced with 300 μM IPTG and lasted overnight at 18 °C at 200 rpm.

Cell pellets were resuspended in lysis buffer (50 mM HEPES pH 7.5, 500 mM NaCl, 5% Glycerol, 10 mM Imidazole, 0.5 mM TCEP) with protease inhibitors (Merck Protease inhibitor cocktail III, 1:500). Sonicated for 15 min 1 s on 1 s off and clarified by centrifugation at 160000×*g* for 30 min. A batch binding of 40 min with 5 ml of Ni-sepharose (cytiva) was performed with the supernatant. The tubes containing the lysate were centrifuged at 700×*g* at 4 °C for 5 min and the supernatant discarded. Beads were loaded on a gravity flow column and washed with 40 ml lysis buffer. 25 ml wash buffer (50 mM HEPES pH 7.5, 500 mM NaCl, 5% Glycerol, 45 mM Imidazole, 0.5 mM TCEP). A further wash with 10 ml Hi-salt buffer (50 mM HEPES pH 7.5, 1 M NaCl, 5% Glycerol, 0.5 mM TCEP) and again with another 10 ml of wash buffer. Proteins were eluted with addition of 15 ml of elution buffer (50 mM HEPES pH 7.5, 500 mM NaCl, 5% Glycerol, 300 mM Imidazole, 0.5 mM TCEP). The elution fraction was analyzed for purity by SDS page and clean fractions were pooled and dialyzed against a desalting buffer containing 25 mM HEPES pH 7.5, 250 mM NaCl, 20% Glycerol, 0.25 mM TCEP. The proteins were stored at −80 °C.

5.8. Determination of SARS-CoV-2 nsp13 unwinding-associated activity

The SARS-CoV-2 nsp13 unwinding-associated activity was measured in black 384 well plates (PerkinElmer) as reported (Corona et al., 2022). Briefly, in 40 μl reaction volume containing 20 mM Tris–HCl pH 7.2, 50 mM NaCl, 2 μM Hel Capture oligo (5′- TGG TGC TCG AAC AGT GAC -3′) from Biomers, 5 mM $MgCl_2$, 10 μg/ml of BSA and 180 μM TCEP, 5% DMSO or inhibitor and 1 nM of purified nsp13 were added. The reaction mixture containing the enzyme was pre-incubated for 10 min with inhibitor at room temperature (RT). The reaction was started adding 1 mM ATP and 750 nM annealed DNA substrate (5′- AGT CTT CTC CTG GTG CTC GAA CAG TGA C-Cy3-3′, 5′- BHQ-2-GTC ACT GTT CGA GCA CCA CCT CTT CTG A-3′) from Biomers. After 15 min of incubation at 37 °C, products were measured with Victor Nivo (Perkin) at 530/580 nm.

5.9. Determination of SARS-CoV-2 nsp13 ATPase-associated activity

The SARS-CoV-2 nsp13 Helicase-associated activity was measured in a transparent 96 well plate (PerkinElmer) as reported (Corona et al., 2022). Briefly,in 25 μl reaction volume containing 20 mM Tris–HCl pH 7.2, 50 mM NaCl, 2 mM $MgCl_2$, 10 μg/ml of BSA and 180 μM TCEP, 5% DMSO or inhibitor and 25 nM of purified nsp13 were added. The reaction was started adding 400 μM ATP. After 30 min of incubation at 37 °C, 50 μl of Biomol® Green Reagent (Prod. No. BML-AK111. Enzo Life-science) were added and reaction was incubated for 10 min at RT, protected from the light. Products were measured with Victor Nivo (Perkin) at 650 nm.

5.10. Data analysis

Data analysis of assay development results was performed using GraphPad Prism Version 9.1.2. Test compound results were normalized relative to respective controls. Dose response curves were fitted to a non-linear regression of (log_{10}) dose vs normalized response-variable slope. Assay quality was assessed using the Z′-factor calculation with $Z' > 0.5$ as threshold for acceptance.

5.11. Binding site identification and molecular docking

GENEOnet tool was applied to identify “druggable” protein binding pockets (Bocchi et al., 2022). GENEOnet is a Dompé farmaceutici SpA proprietary software that combines the geometric and explainability properties of GENEOs with a network architecture into a novel knowledge-based machine learning paradigm. GENEOnet incorporates knowledge such as lipophilicity, hydrophilicity, electrostatic information, necessary to identify a binding site, so we define a GENEO (Bergomi et al., 2019) for each chemical-physical parameter, which can identify areas with the best values for these values. The software compute useful information, such as pocket’s location and their druggability scores (goes from 0 to 1.0, where 1.0 is a high druggable site), useful for in silico studies.

The nsp13 3D structure has been prepared using the Protein Preparation Wizard of Schrodinger, while molecular docking experiments of **1a**, **1b** and SSYA10, into the new identified allosteric binding site, was performed using LiGen™ software (Beato et al., 2013).

Fundings

This research was supported by EU funding within the NextGenerationEU-MUR PNRR Extended Partnership initiative on Emerging Infectious Diseases (Project no. PE00000007, INF-ACT) This publication was supported by the European Virus Archive GLOBAL (EVA-GLOBAL) project that has received funding from the European Union's Horizon 2020 research and innovation program under grant agreement No 871029.

Author contributions

AC[a], VNM[b], RDS[c], RE[a], DI[b], carried out biochemical, and biological experiments, CM[d], DI[d], CT[d], performed the docking simulations and analyzed the data. AC[a], VNM[b], DM[c], GF[c], MA[e], FL[c], interpreted the results outcomes, AC[a], RDS[b], RC[b] and ET[a] devised, conceived and designed the project. MA gave strategic input. The manuscript was written through contributions of all authors and all authors have given approval to the final version of the manuscript.

Declaration of competing interest

The authors declare that they have no known competing financial interests or personal relationships that could have appeared to influence the work reported in this paper.

Data availability

Data will be made available on request.

Acknowledgements

COVID-SARS2 NSP13 was a gift from Opher Gileadi (Addgene plasmid # 159614; http://n2t.net/addgene:159614; RRID:Addgene_159614). We thank prof Pierre-Olivier Vidalain, Centre International de Recherche en Infectiologie, Université Lyon, Inserm, U1111, Université Claude Bernard Lyon 1, CNRS, Lyon, France for providing the BEAS-2B cell line.

Abbreviations

SARS-CoV-2	(severe acute respiratory syndrome coronavirus 2)
RdRp	(RNA-dependent RNA polymerase)
nsp13	(non-structural protein 13)
RTC	(replication-transcription complex)
DKAs	(diketo acid derivatives)

References

Adedeji, A.O., Singh, K., Calcaterra, N.E., DeDiego, M.L., Enjuanes, L., Weiss, S., Sarafianos, S.G., 2012. Severe acute respiratory syndrome coronavirus replication inhibitor that interferes with the nucleic acid unwinding of the viral helicase. Antimicrob. Agents Chemother. 56, 4718–4728. https://doi.org/10.1128/AAC.00957-12.

Adedeji, A.O., Singh, K., Kassim, A., Coleman, C.M., Elliott, R., Weiss, S.R., Frieman, M.B., Sarafianos, S.G., 2014. Evaluation of SSYA10-001 as a replication inhibitor of severe acute respiratory syndrome, mouse hepatitis, and Middle East respiratory syndrome coronaviruses. Antimicrob. Agents Chemother. 58, 4894–4898. https://doi.org/10.1128/AAC.02994-14.

Beato, C., Beccari, A.R., Cavazzoni, C., Lorenzi, S., Costantino, G., 2013. Use of experimental design to optimize docking performance: the case of LiGenDock, the docking module of ligen, a new de novo design program. J. Chem. Inf. Model. 53, 1503–1517. https://doi.org/10.1021/ci400079k.

Bergomi, M.G., Frosini, P., Giorgi, D., Quercioli, N., 2019. Towards a topological–geometrical theory of group equivariant non-expansive operators for data analysis and machine learning. Nat. Mach. Intell. 1, 423–433. https://doi.org/10.1038/s42256-019-0087-3.

Bocchi, G., Frosini, P., Micheletti, A., Pedretti, A., Gratteri, C., Lunghini, F., Beccari, A.R., Talarico, C., 2022. GENEOnet: a new machine learning paradigm based on Group Equivariant Non-Expansive Operators. An application to protein pocket detection. https://doi.org/10.48550/arxiv.2202.00451.

Chen, J., Malone, B., Llewellyn, E., Grasso, M., Shelton, P.M.M., Olinares, P.D.B., Maruthi, K., Eng, E.T., Vatandaslar, H., Chait, B.T., Kapoor, T.M., Darst, S.A., Campbell, E.A., 2020a. Structural basis for helicase-polymerase coupling in the SARS-CoV-2 replication-transcription complex. Cell 182. https://doi.org/10.1016/j.cell.2020.07.033, 1560-1573.e13.

Chen, J., Malone, B., Llewellyn, E., Grasso, M., Shelton, P.M.M., Olinares, P.D.B., Maruthi, K., Eng, E.T., Vatandaslar, H., Chait, B.T., Kapoor, T.M., Darst, S.A., Campbell, E.A., 2020b. Structural basis for helicase-polymerase coupling in the SARS-CoV-2 replication-transcription complex. Cell 182. https://doi.org/10.1016/j.cell.2020.07.033, 1560-1573.e13.

Chen, J., Wang, Q., Malone, B., Llewellyn, E., Pechersky, Y., Maruthi, K., Eng, E.T., Perry, J.K., Campbell, E.A., Shaw, D.E., Darst, S.A., 2022a. Ensemble cryo-EM reveals conformational states of the nsp13 helicase in the SARS-CoV-2 helicase replication–transcription complex. Nat. Struct. Mol. Biol. 250–260. https://doi.org/10.1038/s41594-022-00734-6, 2022 293 29.

Chen, J., Wang, Q., Malone, B., Llewellyn, E., Pechersky, Y., Maruthi, K., Eng, E.T., Perry, J.K., Campbell, E.A., Shaw, D.E., Darst, S.A., 2022b. Ensemble cryo-EM reveals conformational states of the nsp13 helicase in the SARS-CoV-2 helicase replication–transcription complex. Nat. Struct. Mol. Biol. 29, 250–260. https://doi.org/10.1038/s41594-022-00734-6.

Chen, N., Zhou, M., Dong, X., Qu, J., Gong, F., Han, Y., Qiu, Y., Wang, J., Liu, Y., Wei, Y., Xia, J., Yu, T., Zhang, X., Zhang, L., 2020. Epidemiological and clinical characteristics of 99 cases of 2019 novel coronavirus pneumonia in Wuhan, China: a descriptive study. Lancet (London, England) 6736, 1–7. https://doi.org/10.1016/S0140-6736(20)30211-7.

Corona, A., Ballana, E., Distinto, S., Rogolino, D., Vecchio, C. Del, Carcelli, M., Badia, R., Riveira-Muñoz, E., Esposito, F., Parolin, C., Esté, J.A., Grandi, N., Tramontano, E., 2020. Targeting HIV-1 RNase H: N'-(2-Hydroxy-benzylidene)-3,4,5-Trihydroxybenzoylhydrazone as selective inhibitor active against NNRTIs-resistant variants. Viruses 12 (729 12), 729. https://doi.org/10.3390/V12070729, 2020.

Corona, A., di Leva, F.S., Rigogliuso, G., Pescatori, L., Noemi, V., Subra, F., Delelis, O., Esposito, F., Cadeddu, M., Costi, R., Cosconati, S., Novellino, E., Tramontano, E., 2016. New insights into the interaction between pyrrolyl diketoacids and HIV-1 integrase active site and comparison with RNase H. Antivir. Res. 134, 236–243. https://doi.org/10.1016/j.antiviral.2016.09.008.

Corona, A., Di Leva, F.S., Thierry, S., Pescatori, L., Cuzzucoli Crucitti, G., Subra, F., Delelis, O., Esposito, F., Rigogliuso, G., Costi, R., Cosconati, S., Novellino, E., Di Santo, R., Tramontano, E., 2014. Identification of highly conserved residues involved in inhibition of HIV-1 RNase H function by diketo acid derivatives. Antimicrob. Agents Chemother. 58, 6101–6110. https://doi.org/10.1128/AAC.03605-14.

Corona, A., Wycisk, K., Talarico, C., Manelfi, C., Milia, J., Cannalire, R., Esposito, F., Gribbon, P., Zaliani, A., Iaconis, D., Beccari, A.R., Summa, V., Nowotny, M., Tramontano, E., 2022. Natural compounds inhibit SARS-CoV-2 nsp13 unwinding and ATPase enzyme activities. ACS Pharmacol. Transl. Sci. 5, 226–239. https://doi.org/10.1021/acsptsci.1c00253.

Costi, R., Cuzzucoli Crucitti, G., Pescatori, L., Messore, A., Scipione, L., Tortorella, S., Amoroso, A., Crespan, E., Campiglia, P., Maresca, B., Porta, A., Granata, I., Novellino, E., Gouge, J., Delarue, M., Maga, G., Di Santo, R., 2013a. New nucleotide-competitive non-nucleoside inhibitors of terminal deoxynucleotidyl transferase: discovery, characterization, and crystal structure in complex with the target. J. Med. Chem. 56, 7431–7441. https://doi.org/10.1021/jm4010187.

Costi, R., Métifiot, M., Esposito, F., Cuzzucoli Crucitti, G., Pescatori, L., Messore, A., Scipione, L., Tortorella, S., Zinzula, L., Novellino, E., Pommier, Y., Tramontano, E., Marchand, C., Di Santo, R., 2013b. 6-(1-benzyl-1 h -pyrrol-2-yl)-2,4-dioxo-5-hexenoic acids as dual inhibitors of recombinant HIV-1 integrase and ribonuclease H, synthesized by a parallel synthesis approach. J. Med. Chem. 56, 8588–8598. https://doi.org/10.1021/jm401040b.

Gao, Y., Yan, L., Huang, Y., Liu, F., Zhao, Y., Cao, L., Wang, T., Sun, Q., Ming, Z., Zhang, L., Ge, J., Zheng, L., Zhang, Y., Wang, H., Zhu, Y., Zhu, C., Hu, T., Hua, T., Zhang, B., Yang, X., Li, J., Yang, H., Liu, Z., Xu, W., Guddat, L.W., Wang, Q., Lou, Z., Rao, Z., 2020. Structure of the RNA-dependent RNA polymerase from COVID-19 virus. Science 368, 779–782. https://doi.org/10.1126/SCIENCE.ABB7498.

Gervasoni, S., Vistoli, G., Talarico, C., Manelfi, C., Beccari, A.R., Studer, G., Tauriello, G., Waterhouse, A.M., Schwede, T., Pedretti, A., 2020. A comprehensive mapping of the druggable cavities within the SARS-CoV-2 therapeutically relevant proteins by combining pocket and docking searches as implemented in pockets 2.0. Int. J. Mol. Sci. 21, 1–17. https://doi.org/10.3390/ijms21145152.

Gordon, C.J., Tchesnokov, E.P., Woolner, E., Perry, J.K., Feng, J.Y., Porter, D.P., Götte, M., 2020. Remdesivir is a direct-acting antiviral that inhibits RNA-dependent RNA polymerase from severe acute respiratory syndrome coronavirus 2 with high potency. J. Biol. Chem. https://doi.org/10.1074/jbc.RA120.013679.

Hao, W., Wojdyla, J.A., Zhao, R., Han, R., Das, R., Zlatev, I., Manoharan, M., Wang, M., Cui, S., 2017. Crystal structure of Middle East respiratory syndrome coronavirus helicase. PLoS Pathog. 13, 1–19. https://doi.org/10.1371/journal.ppat.1006474.

Hu, Y., Ma, C., Szeto, T., Hurst, B., Tarbet, B., Wang, J., Boceprevir, 2021, 2021. Boceprevir, calpain inhibitors II and XII, and GC-376 have broad-spectrum antiviral activity against coronaviruses. HACS Infect. Dis. 7 (3), 586–597. https://doi.org/10.1021/acsinfecdis.0c00761.

Jia, Z., Yan, L., Ren, Z., Wu, L., Wang, J., Guo, J., Zheng, L., Ming, Z., Zhang, L., Lou, Z., Rao, Z., 2019. Delicate structural coordination of the severe acute respiratory syndrome coronavirus Nsp13 upon ATP hydrolysis. Nucleic Acids Res. 47, 6538–6550. https://doi.org/10.1093/nar/gkz409.

Keum, Y., Jeong, Y., 2012. Development of chemical inhibitors of the SARS coronavirus : viral helicase as a potential target. Biochem. Pharmacol. 84, 1351–1358. https://doi.org/10.1016/j.bcp.2012.08.012.

Keum, Y.S., Lee, J.M., Yu, M.S., Chin, Y.W., Jeong, Y.J., 2013. Inhibition of SARS coronavirus helicase by baicalein. Bull. Kor. Chem. Soc. 34, 3187–3188. https://doi.org/10.5012/bkcs.2013.34.11.3187.

Krieger, I.V., Freundlich, J.S., Gawandi, V.B., Roberts, J.P., Gawandi, V.B., Sun, Q., Owen, J.L., Fraile, M.T., Huss, S.I., Lavandera, J.L., Ioerger, T.R., Sacchettini, J.C., 2012. Structure-guided discovery of phenyl-diketo acids as potent inhibitors of *M. tuberculosis* malate synthase. Chem. Biol. 19, 1556–1567. https://doi.org/10.1016/j.chembiol2012.09.018.

Kuzikov, M., Costanzi, E., Reinshagen, J., Esposito, F., Vangeel, L., Wolf, M., Ellinger, B., Claussen, C., Geisslinger, G., Corona, A., Iaconis, D., Talarico, C., Manelfi, C., Cannalire, R., Rossetti, G., Gossen, J., Albani, S., Musiani, F., Herzog, K., Ye, Y., Giabbai, B., Demitri, N., Jochmans, D., Jonghe, S. De, Rymenants, J., Summa, V., Tramontano, E., Beccari, A.R., Leyssen, P., Storici, P., Neyts, J., Gribbon, P., Zaliani, A., 2021. Identification of inhibitors of SARS-CoV-2 3CL-Pro enzymatic activity using a small molecule in vitro repurposing screen. ACS Pharmacol. Transl. Sci. https://doi.org/10.1021/acsptsci.0c00216.

Kwong, A.D., Rao, B.G., Jeang, K.T., 2005. Viral and cellular RNA helicases as antiviral targets. Nat. Rev. Drug Discov. https://doi.org/10.1038/nrd1853.

Lee, C., Lee, J.M., Lee, N.R., Jin, B.S., Jang, K.J., Kim, D.E., Jeong, Y.J., Chong, Y., 2009. Aryl diketoacids (ADK) selectively inhibit duplex DNA-unwinding activity of SARS coronavirus NTPase/helicase. Bioorg. Med. Chem. Lett 19, 1636–1638. https://doi.org/10.1016/j.bmcl.2009.02.010.

Lehmann, K.C., Snijder, E.J., Posthuma, C.C., Gorbalenya, A.E., 2015. What we know but do not understand about nidovirus helicases. Virus Res. 202, 12–32. https://doi.org/10.1016/j.virusres.2014.12.001.

Li, G., Hilgenfeld, R., Whitley, R., De Clercq, E., 2023. Therapeutic strategies for COVID-19: progress and lessons learned. Nat. Rev. Drug Discov. 22, 449–475. https://doi.org/10.1038/s41573-023-00672-y.

Lu, L., Peng, Y., Yao, H., Wang, Y., Li, J., Yang, Y., Lin, Z., 2022. Punicalagin as an allosteric NSP13 helicase inhibitor potently suppresses SARS-CoV-2 replication in vitro. Antivir. Res. 206, 105389 https://doi.org/10.1016/j.antiviral.2022.105389.

Ma, C., Sacco, M.D., Hurst, B., Townsend, J.A., Hu, Y., Szeto, T., Zhang, X., Tarbet, B., Marty, M.T., Chen, Y., Wang, J., 2020. Boceprevir, GC-376, and calpain inhibitors II, XII inhibit SARS-CoV-2 viral replication by targeting the viral main protease. Cell Res. 30 (8), 678–692.

Malone, B., Chen, J., Wang, Q., Llewellyn, E., Choi, Y.J., Olinares, P.D.B., Cao, X., Hernandez, C., Eng, E.T., Chait, B.T., Shaw, D.E., Landick, R., Darst, S.A., Campbell, E.A., 2021. Structural basis for backtracking by the SARS-CoV-2 replication-transcription complex. Proc. Natl. Acad. Sci. U. S. A 118. https://doi.org/10.1073/pnas.2102516118.

Manelfi, C., Gossen, J., Gervasoni, S., Talarico, C., Albani, S., Philipp, B.J., Musiani, F., Vistoli, G., Rossetti, G., Beccari, A.R., Pedretti, A., 2021. Combining different docking engines and consensus strategies to design and validate optimized virtual screening protocols for the SARS-CoV-2 3CL protease. Mol 2021. https://doi.org/10.3390/MOLECULES26040797, 26, Page 797 26, 797.

Messore, A., Corona, A., Madia, V.N., Saccoliti, F., Tudino, V., De Leo, A., Ialongo, D., Scipione, L., De Vita, D., Amendola, G., Novellino, E., Cosconati, S., Métifiot, M., Andreola, M.-L., Esposito, F., Grandi, N., Tramontano, E., Costi, R., Di Santo, R., 2021. Quinolinonyl non-diketo acid derivatives as inhibitors of HIV-1 ribonuclease H and polymerase functions of reverse transcriptase. J. Med. Chem. https://doi.org/10.1021/acs.jmedchem.1c00535.

Messore, A., Corona, A., Madia, V.N., Saccoliti, F., Tudino, V., De Leo, A., Scipione, L., De Vita, D., Amendola, G., Di Maro, S., Novellino, E., Cosconati, S., Métifiot, M., Andreola, M.-L., Valenti, P., Esposito, F., Grandi, N., Tramontano, E., Costi, R., Di Santo, R., 2020. Pyrrolyl Pyrazoles as Non-Diketo Acid Inhibitors of the HIV-1 Ribonuclease H Function of Reverse Transcriptase. ACS Med. Chem. Lett. doi: acsmedchemlett.9b00617.

Minskaia, E., Hertzig, T., Gorbalenya, A.E., Campanacci, V., Cambillau, C., Canard, B., Ziebuhr, J., 2006. Discovery of an RNA virus 3′→5′ exoribonuclease that is critically involved in coronavirus RNA synthesis. Proc. Natl. Acad. Sci. U. S. A 103, 5108–5113. https://doi.org/10.1073/PNAS.0508200103/SUPPL_FILE/08200FIG8.PDF.

Newman, J.A., Douangamath, A., Yadzani, S., Yosaatmadja, Y., Aimon, A., Brandão-Neto, J., Dunnett, L., Gorrie-stone, T., Skyner, R., Fearon, D., Schapira, M., von Delft, F., Gileadi, O., 2021. Structure, mechanism and crystallographic fragment screening of the SARS-CoV-2 NSP13 helicase. Nat. Commun. 12, 1–11. https://doi.org/10.1038/s41467-021-25166-6.

Nizi, M.G., Persoons, L., Corona, A., Felicetti, T., Cernicchi, G., Massari, S., Manfroni, G., Vangeel, L., Barreca, M.L., Esposito, F., Jochmans, D., Milia, J., Cecchetti, V., Schols, D., Neyts, J., Tramontano, E., Sabatini, S., De Jonghe, S., Tabarrini, O., 2022. Discovery of 2-phenylquinolines with broad-spectrum anti-coronavirus activity. ACS Med. Chem. Lett. https://doi.org/10.1021/acsmedchemlett.2c00123.

Owen, D.R., Allerton, C.M.N., Anderson, A.S., Aschenbrenner, L., Avery, M., Berritt, S., Boras, B., Cardin, R.D., Carlo, A., Coffman, K.J., Dantonio, A., Di, L., Eng, H., Ferre, R.A., Gajiwala, K.S., Gibson, S.A., Greasley, S.E., Hurst, B.L., Kadar, E.P., Kalgutkar, A.S., Lee, J.C., Lee, J., Liu, W., Mason, S.W., Noell, S., Novak, J.J., Obach, R.S., Ogilvie, K., Patel, N.C., Pettersson, M., Rai, D.K., Reese, M.R., Sammons, M.F., Sathish, J.G., Singh, R.S.P., Steppan, C.M., Stewart, A.E., Tuttle, J. B., Updyke, L., Verhoest, P.R., Wei, L., Yang, Q., Zhu, Y., 2021. An oral SARS-CoV-2 Mpro inhibitor clinical candidate for the treatment of COVID-19. Science 80 (374), 1586–1593. https://doi.org/10.1126/science.abl4784.

Perez-Lemus, G.R., Menéndez, C.A., Alvarado, W., Byléhn, F., De Pablo, J.J., 2022a. Toward wide-spectrum antivirals against coronaviruses: molecular characterization of SARS-CoV-2 NSP13 helicase inhibitors. Sci. Adv. 8, 1–13. https://doi.org/10.1126/sciadv.abj4526.

Perez-Lemus, G.R., Menéndez, C.A., Alvarado, W., Byléhn, F., De Pablo, J.J., 2022b. Toward wide-spectrum antivirals against coronaviruses: molecular characterization of SARS-CoV-2 NSP13 helicase inhibitors. Sci. Adv. 8 https://doi.org/10.1126/sciadv.abj4526.

Saikrishnan, K., Powell, B., Cook, N.J., Webb, M.R., Wigley, D.B., 2009. Mechanistic basis of 5′-3′ translocation in SF1B helicases. Cell 137, 849–859. https://doi.org/10.1016/j.cell.2009.03.036.

Singleton, M.R., Dillingham, M.S., Wigley, D.B., 2007. Structure and mechanism of helicases and nucleic acid translocases. Annu. Rev. Biochem. https://doi.org/10.1146/annurev.biochem.76.052305.115300.

Sluis-Cremer, N., Arion, D., Abram, M.E., Parniak, M. a, 2004. Proteolytic processing of an HIV-1 pol polyprotein precursor: insights into the mechanism of reverse transcriptase p66/p51 heterodimer formation. Int. J. Biochem. Cell Biol. 36, 1836–1847. https://doi.org/10.1016/j.biocel.2004.02.020.

Spratt, A.N., Gallazzi, F., Quinn, T.P., Lorson, C.L., Sönnerborg, A., Singh, K., 2021. Coronavirus helicases: attractive and unique targets of antiviral drug-development and therapeutic patents. Expert Opin. Ther. Pat. 31, 339–350. https://doi.org/10.1080/13543776.2021.1884224.

Summa, V., Petrocchi, A., Bonelli, F., Crescenzi, B., Donghi, M., Ferrara, M., Fiore, F., Gardelli, C., Gonzalez Paz, O., Hazuda, D.J., Jones, P., Kinzel, O., Laufer, R., Monteagudo, E., Muraglia, E., Nizi, E., Orvieto, F., Pace, P., Pescatore, G., Scarpelli, R., Stillmock, K., Witmer, M.V., Rowley, M., 2008. Discovery of raltegravir, a potent, selective orally bioavailable HIV-integrase inhibitor for the treatment of HIV-AIDS infection. J. Med. Chem. 51, 5843–5855. https://doi.org/10.1021/jm800245z.

Tomassini, J., Selnick, H., Davies, M.E., Armstrong, M.E., Baldwin, J., Bourgeois, M., Hastings, J., Hazuda, D., Lewis, J., McClements, W., 1994. Inhibition of cap (m7GpppXm)-dependent endonuclease of influenza virus by 4-substituted 2,4-dioxobutanoic acid compounds. Antimicrob. Agents Chemother. 38, 2827–2837.

Tramontano, E., Esposito, F., Badas, R., Di Santo, R., Costi, R., La Colla, P., 2005. 6-[1-(4-Fluorophenyl)methyl-1H-pyrrol-2-yl)]-2,4-dioxo-5-hexenoic acid ethyl ester a novel diketo acid derivative which selectively inhibits the HIV-1 viral replication in cell culture and the ribonuclease H activity in vitro. Antivir. Res. 65, 117–124. https://doi.org/10.1016/j.antiviral.2004.11.002.

V'kovski, P., Kratzel, A., Steiner, S., Stalder, H., Thiel, V., 2020. Coronavirus biology and replication: implications for SARS-CoV-2. Nat. Rev. Microbiol. https://doi.org/10.1038/s41579-020-00468-6.

Wai, J.S., Egbertson, M.S., Payne, L.S., Fisher, T.E., Embrey, M.W., Tran, L.O., Melamed, J.Y., Langford, H.M., Guare, J.P., Zhuang, L., Grey, V.E., Vacca, J.P., Holloway, M.K., Naylor-Olsen, A.M., Hazuda, D.J., Felock, P.J., Wolfe, A.L., Stillmock, K.A., Schleif, W.A., Gabryelski, L.J., Young, S.D., 2000. 4-Aryl-2,4-dioxobutanoic acid inhibitors of HIV-1 integrase and viral replication in cells. J. Med. Chem. 43, 4923–4926.

Wang, L., Sarafianos, S.G., Wang, Z., 2020. Cutting into the substrate dominance: pharmacophore and structure-based approaches toward inhibiting human immunodeficiency virus reverse transcriptase-associated ribonuclease H. Acc. Chem. Res. 53, 218–230. https://doi.org/10.1021/acs.accounts.9b00450.

White, M.A., Lin, W., Cheng, X., 2020. Discovery of COVID-19 inhibitors targeting the SARS-CoV-2 Nsp13 helicase. J. Phys. Chem. Lett. 9144–9151. https://doi.org/10.1021/acs.jpclett.0c02421.

Wu, A., Peng, Y., Huang, B., Ding, X., Wang, X., Niu, P., Meng, J., Zhu, Z., Zhang, Z., Wang, J., Sheng, J., Quan, L., Xia, Z., Tan, W., Cheng, G., Jiang, T., 2020. Genome composition and divergence of the novel coronavirus (2019-nCoV) originating in China. Cell Host Microbe. https://doi.org/10.1016/j.chom.2020.02.001.

Wu, F., Zhao, S., Yu, B., Chen, Y.M., Wang, W., Song, Z.G., Hu, Y., Tao, Z.W., Tian, J.H., Pei, Y.Y., Yuan, M.L., Zhang, Y.L., Dai, F.H., Liu, Y., Wang, Q.M., Zheng, J.J., Xu, L., Holmes, E.C., Zhang, Y.Z., 2020. A new coronavirus associated with human respiratory disease in China. Nature 579, 265–269. https://doi.org/10.1038/s41586-020-2008-3.

Yan, L., Ge, J., Zheng, L., Zhang, Y., Gao, Y., Wang, T., Huang, Y., Yang, Y., Gao, S., Li, M., Liu, Z., Wang, H., Li, Y., Chen, Y., Guddat, L.W., Wang, Q., Rao, Z., Lou, Z., 2021. Cryo-EM structure of an extended SARS-CoV-2 replication and transcription complex reveals an intermediate state in cap synthesis. Cell 184. https://doi.org/10.1016/J.CELL.2020.11.016, 184-193.e10.

Yonetani, T., Rate, I., Methods, I., 1982. The Yonetani-Theorell graphical method for examining overlapping subsites of enzyme active centers. Methods Enzymol. 87, 500–509. https://doi.org/10.1016/S0076-6879(82)87028-6.

Yu, M.S., Lee, J., Lee, J.M., Kim, Y., Chin, Y.W., Jee, J.G., Keum, Y.S., Jeong, Y.J., 2012. Identification of myricetin and scutellarein as novel chemical inhibitors of the SARS coronavirus helicase, nsP13. Bioorg. Med. Chem. Lett 22, 4049–4054. https://doi.org/10.1016/j.bmcl.2012.04.081.

Yuan, S., Yin, X., Meng, X., Chan, J.F.W., Ye, Z.W., Riva, L., Pache, L., Chan, C.C.Y., Lai, P.M., Chan, C.C.S., Poon, V.K.M., Lee, A.C.Y., Matsunaga, N., Pu, Y., Yuen, C.K., Cao, J., Liang, R., Tang, K., Sheng, L., Du, Y., Xu, W., Lau, C.Y., Sit, K.Y., Au, W.K., Wang, R., Zhang, Y.Y., Tang, Y.D., Clausen, T.M., Pihl, J., Oh, J., Sze, K.H., Zhang, A. J., Chu, H., Kok, K.H., Wang, D., Cai, X.H., Esko, J.D., Hung, I.F.N., Li, R.A., Chen, H., Sun, H., Jin, D.Y., Sun, R., Chanda, S.K., Yuen, K.Y., 2021. Clofazimine broadly inhibits coronaviruses including SARS-CoV-2. Nature 593, 418–423. https://doi.org/10.1038/s41586-021-03431-4.

Zeng, J., Weissmann, F., Bertolin, A.P., Posse, V., Canal, B., Ulferts, R., Wu, M., Harvey, R., Hussain, S., Milligan, J.C., Roustan, C., Borg, A., McCoy, L., Drury, L.S., Kjaer, S., McCauley, J., Howell, M., Beale, R., Diffley, J.F.X., 2021. Identifying SARS-CoV-2 antiviral compounds by screening for small molecule inhibitors of nsp13 helicase. Biochem. J. 478, 2405–2423. https://doi.org/10.1042/BCJ20210201.

Zeng, LF., Zhang, HS., Wang, YH., Sanchez, T., Zheng, YT., Neamati, N., Long, YQ., 2008. Efficient synthesis and utilization of phenyl-substituted heteroaromatic carboxylic acids as aryl diketo acid isosteres in the design of novel HIV-1 integrase inhibitors. Bioorg. Med. Chem. Lett. 18, 4521–4524. https://doi.org/10.1016/j.bmcl.2008.07.047.